

# High-Efficiency III-V Multijunction Solar Cells

---

**J. M. Olson, D. J. Friedman and Sarah Kurtz**

*National Renewable Energy Laboratory, Golden, CO*

## 9.1 INTRODUCTION

The large-scale use of photovoltaics is slowly becoming a reality. Small scale ( $\sim 10$ – $20$  kW) power systems using Si solar cells now compete with fossil-fueled electric generators for remote applications, where “remote” in the United States means less than one kilometer from the electrical grid. The total worldwide solar cell production in the year 2000 was 0.3 GW, mostly in the form of flat-plate Si solar cells. Compared to the PV production capacity 20 years ago, this represents remarkable progress. Silicon solar cells have reached efficiencies exceeding 20%, and the cost has been reduced to under \$10/W. However, in the context of world energy consumption, 0.3 GW is a miniscule number. The problem is related to the diffuse nature of solar radiation. For example, to generate 1 GW of electrical power using Si solar cells requires an aperture area on the order of  $10^7$  m<sup>2</sup>. The main problem is not the land area, but the daunting task of producing  $10^7$  m<sup>2</sup> of what has been termed *solar-grade silicon*, which in reality is virtually indistinguishable from semiconductor-grade silicon. One solution to this problem is to use “concentrator technology.” Here, lenses or mirrors focus the sunlight (usually the direct portion) on a smaller solar cell. The concentration ratio can be as large as 200X to 300X for Si and 1000X to 2000X for a GaAs solar cell. At these concentration ratios, the cost of the cell becomes less important than its efficiency. For example, a GaInP/GaAs/Ge tandem cell with an efficiency of 34% at 1000X and a cost of \$10/cm<sup>2</sup> may be more cost-effective than a Si concentrator cell with an efficiency of 28% at 200X and a cost of \$0.50/cm<sup>2</sup>. The trade-offs are complex and currently not well quantified, but it seems clear that concentrator photovoltaics must be a dominant player if photovoltaics have to supply a significant fraction of the world’s energy needs.

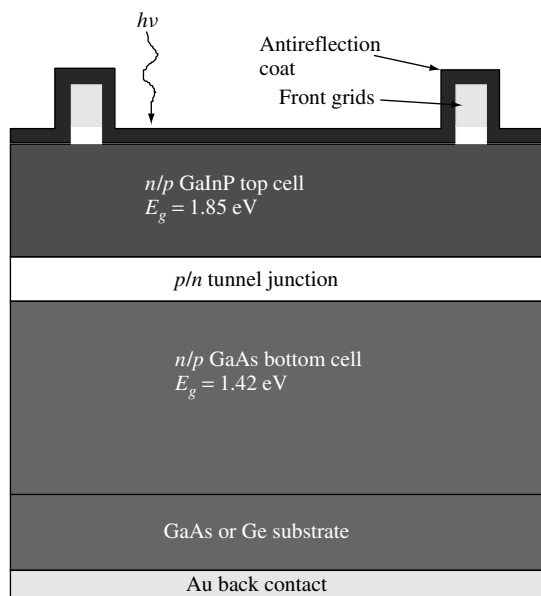


**Figure 9.1** Schematic of GaInP/GaAs multijunction solar cell. When grown on a Ge substrate, there is an option for introducing a third junction in the Ge substrate, thus boosting the voltage and efficiency of the overall device. Dimensions are not to scale

It was in this context that researchers at the National Renewable Energy Laboratory (NREL) conceived and began work on the GaInP/GaAs tandem solar cell more than a decade ago [1]. A schematic of the cell is shown in Figure 9.1. The cell consists of a  $\text{Ga}_x\text{In}_{1-x}\text{P}$  top cell (with a band gap of 1.8–1.9 eV) grown monolithically on a lattice-matched interconnecting tunnel junction and a GaAs bottom cell. As shown in Figure 9.2, for  $x \approx 0.5$ ,  $\text{Ga}_x\text{In}_{1-x}\text{P}$  has the same lattice constant as GaAs with a band gap energy between 1.8 and 1.9 eV. Prior to this, several groups were working on tandem device designs that theoretically should achieve efficiencies approaching 36 to 40% [2]. These included mechanical stacks of a high band gap top cell on a Si bottom cell and monolithic combinations of AlGaAs, GaAs, and GaInAs or GaAsP on Si. However, the mechanical stacks were viewed as too costly and cumbersome (perhaps prematurely). The defects generated by the lattice mismatch between top and bottom cells in some of the monolithic structures (i.e. GaAs and GaInAs or GaAsP and Si) were a problem that could not be solved easily. The AlGaAs/GaAs tandem cell is lattice matched with a theoretical efficiency of 36% [2]. However, the sensitivity of AlGaAs to trace levels of oxygen in all growth systems and source materials made it difficult to produce high yield and, thus, limited its use in a production environment. The novel NREL idea was to trade manufacturability (i.e. lattice-matched top and bottom cells and oxygen-tolerant device materials) for a slightly lower theoretical efficiency of 34%.

By most standards, progress was rapid (see Figure 9.3). Despite initial problems with the growth of GaInP due to metalorganic chemical vapor deposition (MOCVD) and complications associated with an anomalous red shift of the band gap energy, by 1988 reasonably good GaInP top cells could be fabricated [3–5]. In 1990, efficiencies greater

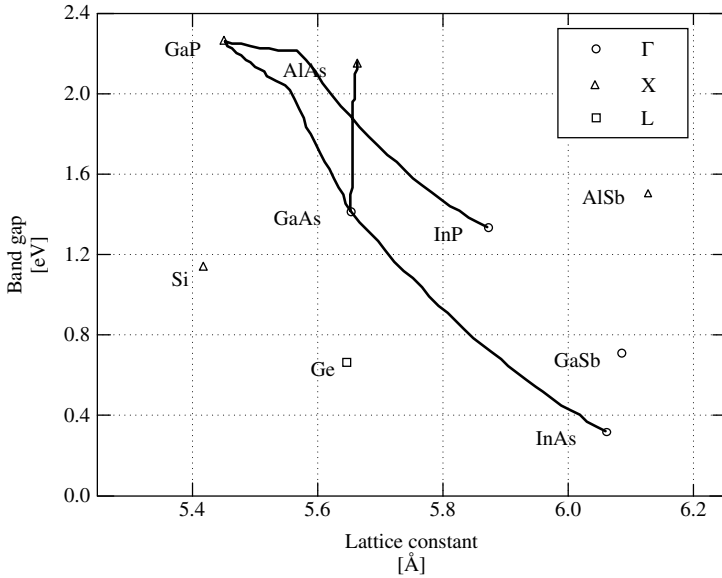


**Figure 9.2** Estimated band gap as a function of lattice constant for Si, Ge, III-V binaries and their alloys

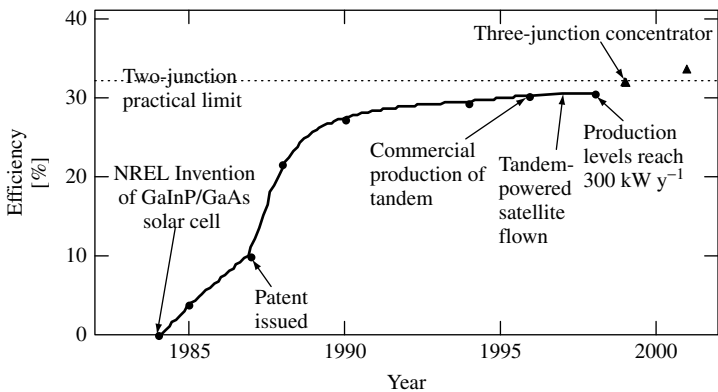


**Figure 9.3** These GaInP/GaAs cell efficiencies were measured at one sun with the AM1.5 global spectrum. The triangles were measured under concentrated sunlight for three-junction GaInP/GaAs/Ge cells

than 27% one-sun air mass 1.5 global (AM1.5G) were achieved by changing the top-cell thickness to achieve current matching [6, 7]. This tuning of the top-cell thickness can also be used to achieve current matching under different solar spectra, for example, AM0 and AM1.5direct (AM1.5D). Using this feature of the GaInP/GaAs tandem solar cell, NREL, over the next three years, set records at AM1.5G with an efficiency  $\eta = 29.5\%$  [8], at 160-suns AM1.5D with  $\eta = 30.2\%$ , [9] and at one-sun AM0 with  $\eta = 25.7\%$  [10]. Soon, numerous laboratories around the world were studying this device, and the 29.5% record was eventually eclipsed by researchers at the Japan Energy Corporation with an efficiency

**Table 9.1** Record solar cell efficiencies. Unless otherwise specified, the cells were fabricated from single crystal materials and the measurements were two-terminal [12]

| Cell             | Efficiency [%] | Area [cm <sup>2</sup> ] | Intensity [suns] | Spectrum | Description                               |
|------------------|----------------|-------------------------|------------------|----------|---|
| GaAs             | 25.1 ± 0.8     | 3.9                     | 1                | Global   | Kopin, AlGaAs window                      |
| GaAs (thin film) | 23.3 ± 0.7     | 4.0                     | 1                | Global   | Kopin, 5-mm                               |
| GaAs(poly)       | 18.2 ± 0.5     | 4.0                     | 1                | Global   | Res. Triangle Inst. (RTI)<br>Ge substrate |
| InP              | 21.9 ± 0.7     | 4.0                     | 1                | Global   | Spire, epitaxial                          |
| GaInP/GaAs       | 30.3           | 4.0                     | 1                | Global   | Japan Energy                              |
| GaInP/GaAs/Ge    | 28.7 ± 1.4     | 29.93                   | 1                | Global   | Spectrolab                                |
| Si               | 24.7 ± 0.5     | 4.0                     | 1                | Global   | UNSW, PERL                                |
| GaAs             | 27.6 ± 1.0     | 0.13                    | 255              | Direct   | Spire                                     |
| GaInAsP          | 27.5 ± 1.4     | 0.08                    | 171              | Direct   | NREL, ENTECH cover                        |
| InP              | 24.3 ± 1.2     | 0.08                    | 99               | Direct   | NREL, ENTECH cover                        |
| GaInP/GaAs/Ge    | 32.4 ± 2.0     | 0.1025                  | 414              | Direct   | Spectrolab                                |
| GaAs/GaSb        | 32.6 ± 1.7     | 0.053                   | 100              | Direct   | Boeing, four-terminal<br>mechanical stack |
| InP/GaInAs       | 31.8 ± 1.6     | 0.063                   | 50               | Direct   | NREL, three-terminal,<br>monolithic       |
| GaInP/GaAs       | 30.2 ± 1.4     | 0.103                   | 180              | Direct   | NREL, monolithic                          |
| Si               | 26.8 ± 0.8     | 1.6                     | 96               | Direct   | Sunpower, back contact                    |

of 30.3% [11]. The current record solar cell efficiencies for this device, along with the record efficiencies of other multijunction devices, are given in Table 9.1.

In 1994, it was discovered that the GaInP/GaAs tandem cells had very good radiation tolerance for operating in space. Kurtz and coworkers published results for a GaInP/GaAs cell with  $\eta = 19.6\%$  (AM0) after irradiation with 1-MeV electrons at a fluence of  $10^{15}/\text{cm}^2$ , [10] a standard radiation dose used to compare various solar cells. This efficiency was higher than the beginning-of-life efficiency of an unirradiated Si solar cell. These attributes soon attracted the attention of the commercial sector. Production of GaInP/GaAs solar cells (on Ge substrates) began in 1996, and the first GaInP-/GaAs-powered satellite was launched in 1997. Today, the production capacity for these tandem cells is about 0.5 MW/year.

This chapter discusses the principles and operation of multijunction solar cells fabricated from III-V semiconductor compounds and alloys, with a particular emphasis on the GaInP/GaAs tandem cell. III-V semiconductors have several characteristics that make them especially suitable for solar cells. A wide selection of these materials is available with direct band gaps, and therefore, high absorption coefficients, in the  $\sim 1$ - to 2-eV range of interest for solar cells; GaAs, with a band gap of 1.42 eV, and  $\text{Ga}_{0.5}\text{In}_{0.5}\text{P}$ , with a band gap of 1.85 eV, are especially important examples. Both *n*- and *p*-type doping of these materials are generally straightforward, and complex structures made from these materials can be grown with extremely high crystalline and optoelectronic quality by high-volume growth techniques. As a result, III-V cells have achieved the highest single-junction efficiencies. Although these *single-junction* efficiencies are only slightly higher than the impressive efficiencies achieved by the best silicon cells, the ease of fabricating

complex III-V structures (including layers with different band gaps) makes possible the creation of III-V *multijunction* cells with efficiencies in excess of 30%, exceeding that of any single-junction device.

## 9.2 APPLICATIONS

### 9.2.1 Space Solar Cells

The higher efficiencies and radiation resistance of III-V cells have made them attractive as replacements for silicon cells on many satellites and space vehicles. Over the years, GaAs cells have replaced silicon cells on new satellite launches. The GaInP/GaAs/Ge cells are integrated into modules very much like single-junction GaAs solar cells and have the added advantage of operating at high voltage and low current, as well as having excellent radiation resistance. They also have a smaller temperature coefficient than silicon cells, which implies better performance under the operating conditions encountered in space applications. Space applications of GaInP/GaAs/Ge and other III-V solar cells are discussed in detail in Chapter 10.

### 9.2.2 Terrestrial Energy Production

The PV industry currently services a wide range of terrestrial applications, from power for small consumer products to larger grid-connected systems. III-V solar cells are currently too expensive for most one-sun applications. While satellites represent an example of an application for which the extra cost is acceptable, for bulk electricity generation, a concentration of 400 suns or greater may be needed to achieve an acceptable cost. Concentrator cells and systems are discussed in detail in Chapter 11.

The use of GaInP/GaAs/Ge cells in high-concentration (e.g. 1000X) systems has the potential of generating electricity at 7 cents/kWh [13]. The current space-cell production capacity of  $\sim 0.5$  MW/year translates into a 1000X concentrator cell production capacity of  $\sim 0.5$  GW/year. These solar cells have achieved a record efficiency of 34%, measured at 210X under the AM1.5 global spectrum [14]. An outdoor module efficiency for a linear (low X) concentrator has been reported in the range of 25.5 to 29% [15]. The high efficiency, the projected low cost, and the ease with which production of concentrator cells could be initiated with existing production equipment make terrestrial applications attractive for these cells. Nevertheless, considerable industry investment will be required to develop a product that is reliable. The specific issues associated with the development of concentrator solar cells are discussed below.

## 9.3 PHYSICS OF III-V MULTIJUNCTION AND SINGLE-JUNCTION SOLAR CELLS

### 9.3.1 Wavelength Dependence of Photon Conversion Efficiency

As a prelude to the detailed examination of the design and performance of multijunction cells, it is useful to review briefly the fundamental factors that limit the efficiency of

single-junction cells. Consider an ideal single-junction cell with characteristic band gap  $E_g$ . A photon incident on this cell with photon energy  $h\nu > E_g$  will be absorbed and converted to electrical energy, but the excess energy  $h\nu - E_g$  will be lost as heat. The greater  $h\nu$  is in excess of  $E_g$ , the lower is the fraction of that photon's energy that will be converted to electrical energy. On the other hand, a photon of energy  $h\nu < E_g$  will not be absorbed and converted to electrical energy at all. Thus, the efficiency of photon conversion is a maximum efficiency at  $h\nu = E_g$ . Note that this maximum efficiency is less than 100%; the maximum work per absorbed photon is calculated by Henry [16].

Since the solar spectrum is broad, containing photons with energies in the range of about 0 to 4 eV, single-junction solar cell efficiencies are thus inherently limited to significantly less than the efficiency with which monochromatic light can be converted. The solution to this problem is (in principle) simple: rather than trying to convert all the photon energies with one cell with one band gap, divide the spectrum into several spectral regions and convert each with a cell whose band gap is tuned for that region. For instance, suppose the spectrum is divided into three regions  $h\nu_1 - h\nu_2$ ,  $h\nu_2 - h\nu_3$ , and  $h\nu_3 - \infty$ , where  $h\nu_1 < h\nu_2 < h\nu_3$ . The light from these spectral regions would be converted by cells with band gaps  $E_{g1} = h\nu_1$ ,  $E_{g2} = h\nu_2$ , and  $E_{g3} = h\nu_3$ , respectively. The greater the number of spectral regions allowed, the higher the potential overall efficiency.

### 9.3.2 Theoretical Limits to Multijunction Efficiencies

Henry has calculated the limiting terrestrial one-sun efficiencies for conversion with 1, 2, 3, and 36 band gaps; the respective efficiencies are 37, 50, 56, and 72% [16]. The improvement in efficiency on going from one to two band gaps is considerable, but the returns diminish as more band gaps are added. This is fortunate since the practicality of a device with more than four or five junctions is doubtful. Note that the promise of the multijunction efficiency improvements will not be realized unless the band gaps of the multiple junctions are correctly chosen; this choice will be discussed below in detail. Theoretical efficiency limits for multijunction devices based on thermodynamic fundamentals are presented in Chapter 4.

### 9.3.3 Spectrum Splitting

The multijunction approach requires that incident photons be directed onto the junction that is tuned to the photon's energy. Perhaps the conceptually simplest approach would be to use an optically dispersive element such as a prism to spatially distribute photons with different energies to different locations, where the appropriate cells would be placed to collect these photons. This approach is illustrated in Figure 9.4(a). Although conceptually simple, in practice the mechanical and optical complexities of this scheme make it undesirable in most circumstances. A generally preferable approach is to arrange the cells in a stacked configuration, as illustrated in Figure 9.4(b), arranged so that the sunlight strikes the highest band gap first, and then goes to the progressively lower band gap junctions. This arrangement makes use of the fact that junctions act as low-pass photon energy filters, transmitting only the sub-band gap light. Thus, in Figure 9.4(b), photons with  $h\nu > E_{g3}$  get absorbed by that junction, photons with  $E_{g2} < h\nu < E_{g3}$  get absorbed by the  $E_{g2}$  junction, and so on; in other words, the junctions themselves act as optical elements to

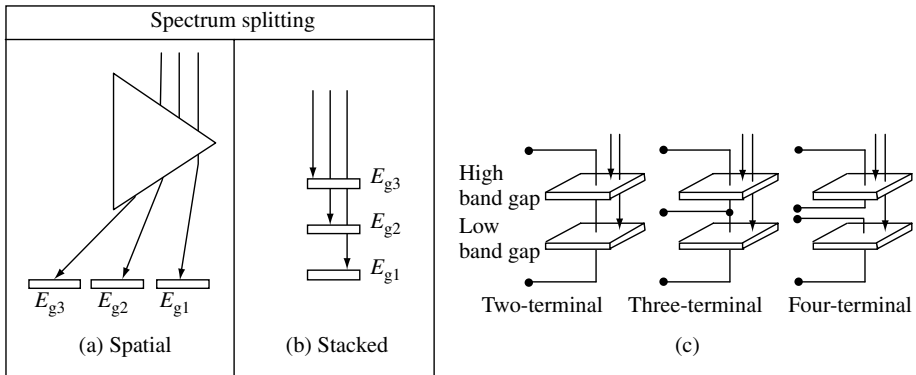


**Figure 9.4** Schematic comparison of (a) spatial-configuration approaches and (b) stacked-configuration approaches to distributing light to subcells of different band gaps. (c) Illustration of two-, three-, and four-terminal connection to a two-junction cell. The figure shows the subcells as mechanically separate, but the two- and three-terminal devices can be monolithic

distribute the spectrum to the appropriate junctions for multijunction photoconversion. The band gaps *must* decrease from top to bottom of the stack. The stacked arrangement avoids the necessity for a separate optical element such as a prism to distribute the spectrum. Also, even if the junctions are physically separate from each other, they can be mechanically brought together into a relatively compact package, called a *mechanical stack*. The stacked configuration requires, of course, that all the junctions in the stack except the bottom one be transparent to light below their band gaps, which, in practice, can set challenging constraints on the substrates and the back-contact metallizations of these junctions through which sub-band gap light must pass. An elegant approach to this problem, which has several other advantages as well, is to fabricate all the junctions, each one atop the last, monolithically on a single substrate. This monolithic-stack approach will be the emphasis of this chapter.

## 9.4 CELL CONFIGURATION

### 9.4.1 Four-terminal

There are several ways to connect power leads to the junctions comprising a multijunction stack. These configurations, which provide for varying degrees of electrical isolation of the subcells, are illustrated in Figure 9.4(c) for a two-junction stack. In the four-terminal configuration, each subcell has its own two terminals and is electrically isolated from the other subcells. This configuration has the advantage that it sets no constraints on the polarities ( $p/n$  vs.  $n/p$ ) of the subcells, or on their currents or voltages. However, the terminals and the electrical isolation between subcells in the four-terminal configuration would be very difficult to accomplish monolithically, because it requires a complicated cell structure and processing. Generally, a four-terminal device is, of necessity, a mechanical stack, whose complexities of fabrication and assembly make it a significantly less desirable structure than the monolithic device.

### 9.4.2 Three-terminal Voltage-matched Interconnections

In contrast, in the three-terminal configuration the subcells are not electrically isolated; the bottom of each cell is electrically connected to the top of the cell beneath it. The fabrication of a monolithic three-terminal device is relatively straightforward, although more complex than the fabrication of a two-terminal device. The semiconductor structure must be designed to provide a layer for contact to the intermediate terminal, and to accommodate the processing steps necessary to put the intermediate terminal in place. With this intermediate terminal, the different subcells in the stack do not have to have the same photocurrents. Furthermore, in this three-terminal configuration, the different subcells in the stack may have different polarities, for example,  $p/n$  for the top cell and  $n/p$  for the bottom cell. Module-level interconnection of four- and three-terminal devices is discussed in detail by Gee [17].

### 9.4.3 Two-terminal Series-connected (Current Matched)

The two-terminal series-connected configuration provides the most restrictions for interconnection of the devices. This configuration requires that the subcells be of the same polarity and that the photocurrents of the subcells be closely matched, since in this series connection the subcell with the least photocurrent limits the current generated by the entire device. This current-matching constraint, about which more will be said shortly, puts relatively tight constraints on the selection of band gaps for the various junctions in this structure. Against these disadvantages, however, are critical advantages. The existence of high-quality monolithic tunnel-junction subcell interconnects means that these stacks can be made as monolithic two-junction structures with metallization at the very top and bottom of the stack only. This, in turn, means that such devices can be integrated into modules with the same simplicity afforded by single-junction devices. The two-terminal, series-connected configuration will be the focus of the following sections, in which we analyze in detail the dependence of the cell performance on the cell design parameters.

## 9.5 COMPUTATION OF SERIES-CONNECTED DEVICE PERFORMANCE

### 9.5.1 Overview

This section discusses the quantitative modeling of the performance of series-connected, two-terminal, two-junction devices. This analysis will provide the basis for a qualitative understanding of the general trends in series-connected multijunction devices, as well as the quantitative design of these devices. Emphasis is placed on selecting band gap pairs and predicting the efficiency of the resulting structures. This modeling also lays the groundwork for the analysis of the dependence of the device performance on the spectrum, the concentration, and the temperature. Although the emphasis is on two-junction devices, we will occasionally extend the discussion to the analysis of a three-junction device, GaInP/GaAs/Ge, which is of special interest due to its technical and commercial success in space applications. Following the treatments of References [7, 18], we make



simplifying assumptions, which include (1) transparent zero-resistance tunnel-junction interconnects, (2) no reflection losses, (3) no series-resistance losses, and (4) junctions that collect every absorbed photon, and whose current–voltage ( $J-V$ ) curves are described by the ideal ( $n = 1$ ) diode equation. Later, we relax assumption (2) to analyze the effect of antireflection coatings; the relaxation of the other assumptions is straightforward, as well. It should be noted that high-quality III-V cells have achieved 90% of these predicted efficiencies.

### 9.5.2 Top and Bottom Subcell $QE$ and $J_{SC}$

The short-circuit current density ( $J_{SC}$ ) of each subcell is determined by the quantum efficiency of the subcell,  $QE(\lambda)$ , and by the spectrum of light incident on that cell  $\Phi_{inc}(\lambda)$  in the usual way:

$$J_{SC} = e \int_0^\infty QE(\lambda) \Phi_{inc}(\lambda) d\lambda \quad (9.1)$$

The  $QE$  for an ideal cell of finite base thickness  $x_b$ , emitter thickness  $x_e$ , and depletion width  $W$  (for a total thickness  $x = x_e + W + x_b$ ) is given by the standard equations [19]

$$QE = QE_{emitter} + QE_{depl} + \exp[-\alpha(x_e + W)]QE_{base} \quad (9.2)$$

where

$$QE_{emitter} = f_\alpha(L_e) \left( \frac{\ell_e + \alpha L_e - \exp(-\alpha x_e) \times [\ell_e \cosh(x_e/L_e) + \sinh(x_e/L_e)]}{\ell_e \sinh(x_e/L_e) + \cosh(x_e/L_e)} - \alpha L_e \exp(-\alpha x_e) \right) \quad (9.3)$$

$$QE_{depl} = \exp(-\alpha x_e)[1 - \exp(-\alpha W)] \quad (9.4)$$

$$QE_{base} = f_\alpha(L_b) \left( \alpha L_b - \frac{\ell_b \cosh(x_b/L_b) + \sinh(x_b/L_b) + (\alpha L_b - \ell_b) \exp(-\alpha x_b)}{\ell_b \sinh(x_b/L_b) + \cosh(x_b/L_b)} \right) \quad (9.5)$$

$$\ell_b = S_b L_b / D_b, \ell_e = S_e L_e / D_e, D_b = kT \mu_b / e, D_e = kT \mu_e / e \quad (9.6)$$

$$f_\alpha(L) = \frac{\alpha L}{(\alpha L)^2 - 1} \quad (9.7)$$

The photon wavelength dependence is not explicit in these equations, but enters through the wavelength dependence of the absorption coefficient  $\alpha(\lambda)$ . The quantities  $\mu_{b(e)}$ ,  $L_{b(e)}$ , and  $S_{b(e)}$  are, respectively, the mobility, diffusion length, and surface recombination velocity for the minority carriers in the base (emitter);  $T$  is the absolute temperature. Later in this chapter, we will illustrate the use of these equations in the analysis of real-world III-V cells. However, in this section, we shall make the simplifying assumption that each absorbed photon is converted to photocurrent, a remarkably good first approximation

for high-quality III-V junctions. In this case, the  $QE$  depends very simply on the total thickness of the device,  $x = x_e + W + x_b$ , as

$$QE(\lambda) = 1 - \exp[-\alpha(\lambda)x] \quad (9.8)$$

because a fraction  $\exp[-\alpha(\lambda)x]$  of the incident light is transmitted through the cell instead of being absorbed. [Although this last equation is self-evident, it can also be deduced from equations (9.2)–(9.5) by setting  $S = 0$ ,  $L \gg x$ , and  $L \gg 1/\alpha$ .]

For sub-band gap photons,  $\alpha(\lambda) = 0$ , and thus  $\exp[-\alpha(\lambda)x] = 1$ . The light  $\Phi_{\text{inc}}$  incident on the top cell is simply the solar spectrum,  $\Phi_S$ . In contrast, the light hitting the bottom cell is filtered by the top cell, so that the bottom cell sees an incident spectrum  $\Phi_S \exp[-\alpha_t(\lambda)x_t]$ , where  $x_t$  and  $\alpha_t(\lambda)$  are the top-cell thickness and absorption coefficient, respectively. Assuming that the bottom cell is thick enough to absorb essentially all of the above band gap photons incident on it, we conclude that the short-circuit current densities of the top cell,  $J_{\text{SCt}}$ , and the bottom cell,  $J_{\text{SCb}}$ , are given by

$$J_{\text{SCt}} = e \int_0^{\lambda_t} (1 - \exp[-\alpha_t(\lambda)x_t]) \Phi_S(\lambda) d\lambda, \quad J_{\text{SCb}} = e \int_0^{\lambda_b} \exp[-\alpha_t(\lambda)x_t] \Phi_S(\lambda) d\lambda \quad (9.9)$$

where  $\lambda_b = hc/E_{\text{gb}}$  and  $\lambda_t = hc/E_{\text{gt}}$  are the wavelengths corresponding to the band gaps of the bottom and top cells, respectively. The lower limit on the  $J_{\text{SCb}}$  integral is 0, not  $\lambda_t$ , because unless the top cell is infinitely thick, it will transmit some short-wavelength photons to the bottom cell. Because the bottom subcell is filtered by the top subcell,  $J_{\text{SCb}}$  depends on both  $E_{\text{gb}}$  and  $E_{\text{gt}}$ , whereas  $J_{\text{SCt}}$  depends only on  $E_{\text{gt}}$ . Equation (9.10) shows this dependence with special clarity in the case of an infinitely thick top cell. In this case,  $\exp[-\alpha_t(\lambda)x_t] = 0$  for all photon energies above  $E_{\text{gt}}$ , so that the  $J_{\text{SC}}$  equations become

$$J_{\text{SCt}} = e \int_0^{\lambda_t} \Phi_S(\lambda) d\lambda, \quad J_{\text{SCb}} = e \int_{\lambda_t}^{\lambda_b} \Phi_S(\lambda) d\lambda \quad (9.10)$$

### 9.5.3 Multijunction $J$ – $V$ Curves

For any set of  $m$  series-connected subcells (or, indeed, any sort of two-terminal element or device) whose individual current–voltage ( $J$ – $V$ ) curves are described by  $V_i(J)$  for the  $i$ th device, the  $J$ – $V$  curve for the series-connected set is simply

$$V(J) = \sum_{i=1}^m V_i(J) \quad (9.11)$$

that is, the voltage at a given current is equal to the sum of the subcell voltages at that current. Each individual subcell will have its own maximum-power point  $\{V_{\text{mp}_i}, J_{\text{mp}_i}\}$ , which maximizes  $J \times V_i(J)$ . However, in the series-connected multijunction connection of these subcells, the currents through each of the subcells are constrained to have the same value, and therefore *each subcell will be able to operate at its maximum-power point only if  $J_{\text{mp}_i}$  is the same for all the subcells*, that is,  $J_{\text{mp}_1} = J_{\text{mp}_2} = \dots = J_{\text{mp}_m}$ . If this is the case, then the maximum power output of the combined multijunction device is

the sum of the maximum power outputs  $V_{mp_i} J_{mp_i}$  of the subcells. On the other hand, if the subcells do not all have the same value for  $J_{mp_i}$ , then in their series-connected multijunction combination, some of the subcells must necessarily operate away from their maximum-power points.

The consequences of this last point are especially important when, as is the case for high-quality III-V junctions, the subcells do not leak or quickly break down in reverse bias. The adding of series  $J-V$  curves in this case is illustrated graphically in Figure 9.5, which shows  $J-V$  curves for a GaInP top subcell, a GaAs bottom subcell, and the two-junction series-connected combination of these two subcells. In this example, the bottom subcell has a higher  $J_{SC}$  than the top subcell; the top subcell is slightly shunted, to make the illustration of its behavior at the tandem  $J_{SC}$  easier to see. For any given value of current, the tandem voltage satisfies  $V_{tandem} = V_{top} + V_{bottom}$ , as can be verified by the inspection of the figure. The region of current near the tandem cell  $J_{SC} = -14 \text{ mA/cm}^2$ , shown in expanded scale in the bottom panel of the figure, is of special interest. At  $J = -13.5 \text{ mA/cm}^2$ , both subcells are in forward bias, with voltages only slightly less than their respective open-circuit voltages ( $V_{OC}$ s). As the magnitude of the current density is further increased to  $-14 \text{ mA/cm}^2$  and beyond, the bottom subcell remains in forward bias near its  $V_{OC}$ . At the same time, in contrast, the top subcell voltage becomes rapidly more negative, so that at  $J = -14 \text{ mA/cm}^2$ , it has reached a negative bias of about  $-1 \text{ V}$ , equal in magnitude but opposite in sign to the top subcell's forward bias of  $+1 \text{ V}$ . At this

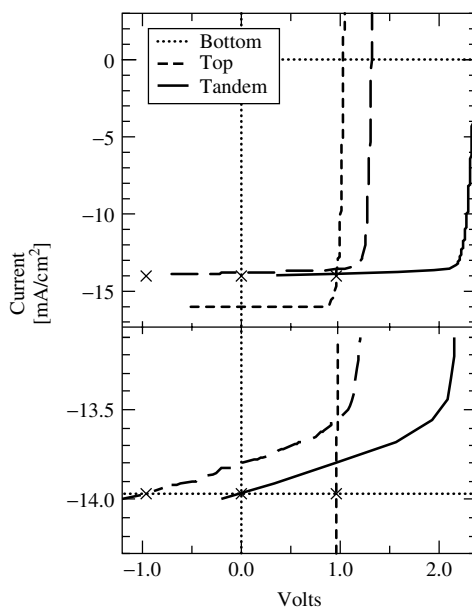


**Figure 9.5** Illustration of the addition of  $J-V$  curves for two series-connected subcells. The lower panel is an expanded view of the current range in the vicinity of the current-limiting top subcell  $J_{SC}$ , showing how the tandem  $J_{SC}$  is limited to the lesser of the subcell currents. The  $J-V$  of the top subcell in this example is slightly leaky, which makes the addition of the subcell  $J-V$  curves near  $J_{SC}$  easier to see. The X's mark voltage of the top, bottom, and tandem when the tandem is at short circuit of  $14 \text{ mA/cm}^2$

value of current, the tandem cell is at zero bias; hence  $J_{SC}$ . This behavior illustrates the general principle that for subcells without significant leakage or reverse-bias breakdown, *the tandem  $J_{SC}$  is constrained to be, to a very good approximation, the lesser of the  $J_{SC}$ s of the subcells.* (Note that this current-limiting characteristic makes series-connected multijunction cells of the type considered here much *worse* than single-junction cells for conversion of narrowband spectra such as the light from a laser! The reader should try to make sure to understand why this is the case.)

To model multijunction devices quantitatively, we need expressions for the subcell  $J-V$  curves,  $V_i(J)$ . To proceed, we use the classical ideal-photodiode  $J-V$  equations (neglecting the depletion region), [19]

$$J = J_0[\exp(eV/kT) - 1] - J_{SC} \quad (9.12)$$

where  $e$  is the electric charge, and we have assumed that the diode ideality factor is 1. An important special case of this is

$$V_{OC} \approx (kT/e) \ln(J_{SC}/J_0) \quad (9.13)$$

because, in practice,  $J_{SC}/J_0 \gg 1$ . The dark current density  $J_0$  is given by

$$J_0 = J_{0,base} + J_{0,emitter} \quad (9.14)$$

where

$$J_{0,base} = e \left( \frac{D_b}{L_b} \right) \left( \frac{n_i^2}{N_b} \right) \left( \frac{(S_b L_b / D_b) + \tanh(x_b / L_b)}{(S_b L_b / D_b) \tanh(x_b / L_b) + 1} \right) \quad (9.15)$$

and a similar equation describes  $J_{0,emitter}$ . The intrinsic carrier concentration  $n_i$  is given by

$$n_i^2 = 4M_c M_v (2\pi kT / h^2)^3 (m_e^* m_h^*)^{3/2} \exp(-E_g / kT) \quad (9.16)$$

where  $m_e^*$  and  $m_h^*$  are the electron and hole effective masses, and  $M_c$  and  $M_v$  are the number of equivalent minima in the conduction and valence bands, respectively.  $N_{b(e)}$  is the base (emitter) ionized-impurity density.

Each junction in a multijunction structure is described by eqs. (9.12)–(9.16); the  $i$ th junction will have dark current  $J_{0,i}$  short-circuit  $J_{SC,i}$  etc, with a corresponding  $J-V$  characteristic  $V_i(J)$ . Adding these  $V_i(J)$  curves for the individual junctions gives the full multijunction  $V(J)$  curve of eq. (9.11). The maximum-power point  $\{J_{mp}, V_{mp}\}$  can be calculated numerically as the point on the  $V(J)$  curve that maximizes  $J \times V(J)$ . The various solar cell performance parameters of interest can be extracted from the  $J-V$  curve in the usual way; for example,  $V_{OC} = V(0)$ ,  $FF = J_{mp} V_{mp} / (V_{OC} J_{SC})$ .

## 9.5.4 Efficiency versus Band Gap

To obtain concrete, numerical values for the cell performance, we need to choose numbers for the material properties of the junctions. Reference [7] provides a reasonable model of a two-junction  $n/p$  cell, in which the bottom junction has the properties of GaAs, except

that the band gap is allowed to vary. The absorption coefficient is shifted rigidly with the band gap so that it correctly goes to zero as the photon energy decreases below the band gap energy. Likewise, for the top subcell, the model uses the material properties of GaInP, again allowing the band gap to vary. The diffusion lengths at 300 K for the GaAs cell are  $L_b = 17 \mu\text{m}$  and  $L_e = 0.8 \mu\text{m}$ ; for the GaInP cell,  $L_b = 3.7 \mu\text{m}$  and  $L_e = 0.6 \mu\text{m}$ . For simplicity, and to give results representing the maximum possible performance, all surface recombination is taken as zero. The emitters for both subcells have thickness  $x_e = 0.1 \mu\text{m}$  and ionized dopant concentration  $N_e = 2 \times 10^{18}/\text{cm}^3$ , and the bases for both subcells have  $N_b = 10^{17}/\text{cm}^3$ . These values are comparable to those used in actual GaInP/GaAs multijunction cells, which provide an optimal combination of high quantum efficiency, low dark current, and low series resistance. Using this model, Figure 9.6(a) plots contours of cell efficiency for a two-junction series-connected cell with infinitely thick subcells, calculated for the one-sun standard AM1.5 global spectrum. Similar contours are shown for a variety of spectra and concentrations by Nell and Barnett [20] and by Wanlass *et al.* [18]. At the optimal band gap combination of  $\{E_{gt} = 1.75 \text{ eV}, E_{gb} = 1.13 \text{ eV}\}$  an efficiency of almost 38% is predicted, well in excess of the 29% efficiency that the model would predict for the best single-junction device.

Even at a bandgap combination of  $\{E_{gt} = 1.95 \text{ eV}, E_{gb} = 1.42 \text{ eV}\}$ , though well away from the optimal bandgap combination, the efficiency is still much higher than the best single-junction efficiency. This band gap pair was chosen for consideration because the bottom-subcell band gap is the band gap of GaAs, while the top-subcell band gap is only slightly higher than the 1.85 eV band gap obtained under typical growth conditions for GaInP. But as  $E_{gt}$  decreases from 1.95 eV to the GaInP band gap of 1.85 eV (with  $E_{gb}$  held at the GaAs band gap of 1.42 eV) the efficiency falls very rapidly, from 35 to 30%. This drop-off is due to the dependence of the top- and bottom-subcell photocurrents

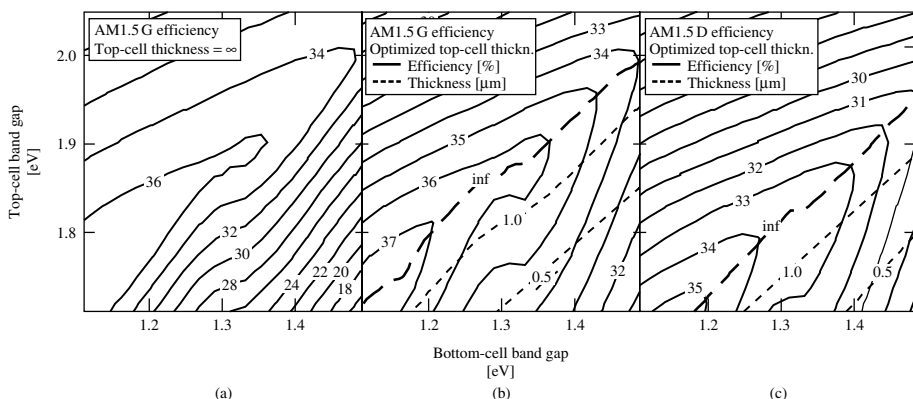


**Figure 9.6** Contour plots of efficiency versus subcell band gaps for a series-connected two-terminal two-junction tandem cell. Adapted from Kurtz S, Faine P and Olson J, *J. Appl. Phys.* **68**, 1890 (1980) [7]. Panel (a) is calculated for the AM1.5 global spectrum, with an infinitely thick top subcell. Panel (b) is calculated for the same spectrum, but for the top subcell thickness that optimizes the tandem-cell efficiency at each combination of top- and bottom-cell band gap; the dashed contours show this optimal thickness. In the region of the graph above the thickness =  $\infty$  contour, the tandem current is limited by the top cell. Panel (c) shows efficiencies and optimal top-cell thicknesses calculated as in (b) but for the AM1.5 direct spectrum

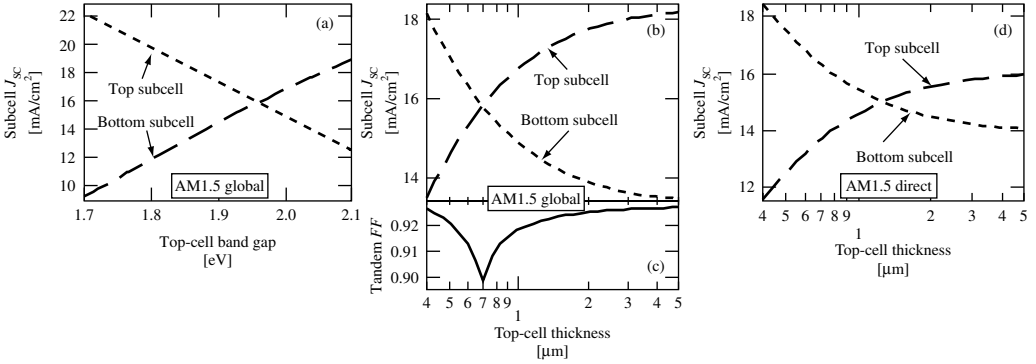


**Figure 9.7** (a)  $J_{SCt}$  and  $J_{SCb}$  for an infinitely thick top subcell as a function of top-subcell band gap  $E_{gt}$  for a bottom-subcell band gap  $E_{gb} = 1.42$  eV. (b)  $J_{SCt}$  and  $J_{SCb}$  as a function of top-subcell thickness for the AM1.5 global spectrum, with  $E_{gb} = 1.42$  eV and  $E_{gt} = 1.85$  eV. The subcells are current matched at a base thickness of  $0.7 \mu\text{m}$ . (c) The corresponding tandem-cell fill factor. (d)  $J_{SCt}$  and  $J_{SCb}$  as a function of top-subcell thickness as in (b) but for the AM1.5 direct spectrum. The current-matching thickness is significantly greater than that for the global spectrum

on the top-subcell band gap. As noted above, lowering the top-subcell band gap while holding the bottom-subcell band gap constant increases the top-subcell  $J_{SC}$  at the expense of the bottom-subcell  $J_{SC}$ . Figure 9.7(a) illustrates this for the case at hand by showing  $J_{SCt}$  and  $J_{SCb}$  as a function of  $E_{gt}$  for  $E_{gb} = 1.42$  eV. The  $J_{SC}$  for the series-connected combination of these two cells will be the lesser of  $J_{SCt}$  and  $J_{SCb}$ . The figure shows that this quantity is a maximum at the current-matched band gap  $E_{gt} = 1.95$  eV, and falls off rapidly as  $E_{gt}$  decreases below 1.95 eV. This falloff in  $J_{SC}$  due to the bottom subcell limiting the photocurrent at low  $E_{gt}$  is responsible for the corresponding drop-off in the tandem-cell efficiency shown in Figure 9.6(a). This dependence of tandem  $J_{SC}$  and efficiency on  $E_{gt}$  would suggest that a GaInP/GaAs cell would not have a useful high efficiency. Fortunately, as will be discussed in the next section, this rapid drop-off of efficiency can be greatly alleviated by thinning the top subcell.

### 9.5.5 Top-cell Thinning

Because the absorption coefficient  $\alpha(h\nu)$  for solar cell materials is not infinite, a cell of finite thickness will not absorb all the incident above band gap light. Some light will be transmitted (especially at photon energies near the band gap where  $\alpha$  is small); the thinner the cell, the greater the transmission. Therefore, for a two-junction cell, thinning the top subcell will reappportion the light between the two subcells, increasing the bottom-subcell current at the expense of the top-subcell current. If, before thinning,  $J_{SCb} < J_{SCt}$ , then the top subcell can be thinned to make  $J_{SCb} = J_{SCt}$ . Because the series-multijunction cell current  $J_{SC}$  is limited to the lesser of  $J_{SCb}$  and  $J_{SCt}$ ,  $J_{SC}$  and hence the cell efficiency will be maximized when the top subcell is thinned to achieve this current matching. Figure 9.7(b) illustrates this current matching for the tandem device under discussion, for the case that  $E_{gt} = 1.85$  eV (GaInP) and  $E_{gb} = 1.42$  eV (GaAs). The tandem current  $J_{SC} \approx \min(J_{SCt}, J_{SCb})$  is maximized at a top-subcell thickness of  $0.7 \mu\text{m}$ , for which the subcells are current matched. At this thickness,  $J_{SC} = J_{SCt} = 15.8 \text{ mA/cm}^2$ , or about 85%

of what  $J_{\text{SCt}}$  would be for an infinite-thickness top subcell. The ability of such a thin cell to absorb such a high fraction of the incident light is due to the large absorption coefficient of this direct gap material.

By comparison with the thinned top-subcell case, for an infinitely thick top subcell the multijunction  $J_{\text{SC}}$  would be determined by the bottom subcell at a current  $J_{\text{SCb}} = 13.4 \text{ mA/cm}^2$ . This improvement in  $J_{\text{SC}}$  on thinning the top cell results in a corresponding improvement in the cell efficiency, from 30% to approximately  $15.8/13.4 * 30\% \approx 35\%$ . This estimate is only approximate because, as will be discussed below, top-cell thinning affects the fill factor and  $V_{\text{OC}}$ , as well as  $J_{\text{SC}}$ . However, these are second-order effects, and the approximation of scaling efficiency with  $J_{\text{SC}}$  alone is quite good. We can see this in Figure 9.6(b), which shows contours of cell efficiency vs. top- and bottom-subcell band gap, for optimal top-subcell thickness. The figure confirms that the cell efficiency at  $\{E_{\text{gt}} = 1.85 \text{ eV } E_{\text{gb}} = 1.42 \text{ eV}\}$  is about 35%. The figure also shows contours of the optimal top-subcell thickness. The optimal thickness decreases with increasing  $E_{\text{gb}}$  or decreasing  $E_{\text{gt}}$ , as required, to maintain current matching. The thick dashed line is the contour of infinite top-subcell thickness; above this contour, the tandem-cell current is always limited by the top subcell, whereas below this contour, thinning the top subcell improves the tandem-cell efficiency. Comparing the optimized efficiencies to the infinite-thickness efficiencies of Figure 9.6(a), we see that the top-subcell thinning greatly reduces the sensitivity of the tandem efficiency on subcell band gap, in effect widening the range of band gaps that can be selected.

### 9.5.6 Current-matching Effect on Fill Factor and $V_{\text{OC}}$

The fill factor (FF) of the tandem cell depends on the top- and bottom-subcell photocurrents. Figure 9.7(c) shows the fill factor as a function of top-cell thickness, and thus effectively as a function of  $J_{\text{SCt}}/J_{\text{SCb}}$ , for the device of Figure 9.7(b). The fill factor is a minimum at the current-matched condition, an effect that holds in general for reasonably ideal (nonleaky) subcells. This effect slightly undermines the efficiency gains that accrue from the increase in  $J_{\text{SC}}$  at the current-matched condition; however, the decrease in fill factor at current matching is roughly half the increase in  $J_{\text{SC}}$ . This dependence of fill factor on the ratio of the subcell currents is important, because it implies that correctly measuring the fill factor of an actual device requires correctly light-biasing the subcells. This subject is discussed further in the chapter on measurements (see Chapter 16).

As equations (9.13–9.15) show,  $V_{\text{OC}}$  also depends on cell thickness. Figure 9.8 shows how finite base thickness  $x_b$  and base surface recombination velocity  $S_b$  affect the  $V_{\text{OC}}$  of a GaInP cell. These curves were calculated using equations (9.13–9.15), assuming a bulk recombination velocity  $D_b/L_b = 2.8 \times 10^4 \text{ cm/s}$ , a typical value for a GaInP cell. The figure shows that for a cell with a well-passivated base, that is,  $S_b$  small enough that  $S_b \ll D_b/L_b$ , thinning the cell results in a meaningful increase in  $V_{\text{OC}}$ . On the other hand, for a cell whose base is so poorly passivated that  $S_b > D_b/L_b$ , thinning the cell lowers  $V_{\text{OC}}$ . For the GaInP/GaAs tandem structure, with the thin top subcell required for current matching, the passivation of the base of the top subcell is thus an important consideration for the overall device efficiency. The passivation of GaInP surfaces will be discussed later in this chapter.

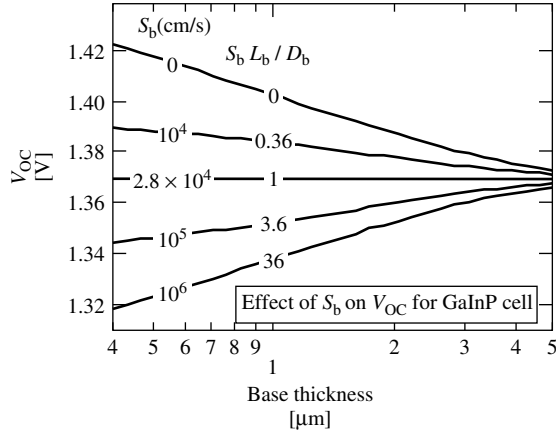


**Figure 9.8** Effect of base thickness  $x_b$  and surface-recombination velocity  $S_b$  on  $V_{OC}$  for a GaInP top cell with  $J_{SC} = 14 \text{ mA/cm}^2$ . The base is characterized by a *bulk* recombination velocity  $D_b/L_b = 2.8 \times 10^4 \text{ cm/s}$ . Note that when the bulk and surface recombination velocities are equal,  $V_{OC}$  is independent of base thickness

### 9.5.7 Spectral Effects

The amount of light distributed to each subcell, and thus, the photocurrents generated by each subcell, is determined by the spectrum of the incident light. (See Chapters 3 and 16 for a more complete discussion of spectra and absorption.) Therefore, the optimal band gaps and the optimal top-subcell thinning depend on the incident spectrum. Figure 9.6(c) shows the efficiency versus top- and bottom-subcell band gap for the standard AM1.5 direct spectrum for the same two-junction device as was modeled for the global spectrum in Figure 9.6(b). For a given bottom-subcell band gap, the optimal top-subcell band gap  $E_{gt}$  is lower for the direct spectrum than for the global spectrum. This difference arises because the direct spectrum has less blue light than the global spectrum, resulting in a diminished  $J_{SCt}/J_{SCb}$ ; lowering  $E_{gt}$  compensates for this by directing more light to the top cell. Likewise, for a given  $E_{gt}$  and  $E_{gb}$ , the optimal top-subcell thickness is greater for the direct spectrum than for the global spectrum. Figure 9.7(d) shows  $J_{SCt}$  and  $J_{SCb}$  for the {1.85, 1.42} eV band gap pairing as a function of top-subcell thickness as in Figure 9.7(a), but calculated for the direct spectrum instead of the global spectrum. The thickness required for current matching is roughly  $1.2 \text{ } \mu\text{m}$ , significantly greater than the  $0.7\text{-}\mu\text{m}$  current-matching thickness for the global spectrum. For comparison, the AM0 spectrum is even more blue-rich than the AM1.5 global spectrum, and the top subcell would correspondingly be thinner, about  $0.5 \text{ } \mu\text{m}$  in thickness.

#### 9.5.7.1 Spectral fluctuations

While the analysis above shows how to choose a top-cell thickness for a given spectrum, no one spectrum precisely represents the actual spectrum seen by a terrestrial solar cell. Fluctuations in the spectrum with time due to the changing position of the sun in the sky, and the changing atmospheric conditions, can be quite significant. The detailed



implications for tandem-cell design are complicated [21]. In general, it is found that series tandem cells are quite sensitive to fluctuations in air mass in particular. Fortunately, efficiency at high air mass is relatively unimportant because the net power output is small under these conditions. Overall, a well-designed multijunction cell is expected to outperform a single-junction cell by a comfortable margin even when spectral fluctuations are taken into account. (It is interesting to note that spectral fluctuations are less of a concern for voltage-matched devices than for current-matched devices, because a change in a subcell current is reflected only logarithmically in the corresponding change in voltage.)

#### 9.5.7.2 Chromatic aberration

A related issue of concern for series-connected multijunction cells is the chromatic aberration of the spectrum that can be caused by the concentrating optics in concentrator modules, especially the Fresnel lenses used by some concentrator configurations. Such aberration will not only change the spectrum from the incident solar spectrum, but may also result in a position-dependent variation in the spectrum across the receiver. It is found that the detrimental effect of such spatial variations may be mitigated by making the emitters of the bottom subcells highly conductive [22]. This aids current matching by lateral conduction between adjacent areas of a cell.

### 9.5.8 AR Coating Effects

#### 9.5.8.1 Introduction

Our discussion has so far assumed for simplicity that there is no reflection of the incident light from the front surface of the cell. However, without an antireflective (AR) coating, III-V cells typically have large reflectances on the order of 30% in the spectral region of importance for converting the solar spectrum. AR coats can reduce this reflectance to  $\sim 1\%$ , but only over a limited spectral range; this limitation has important implications for tandem-cell current matching. An examination of AR coating issues is therefore especially important for III-V multijunction cells.

#### 9.5.8.2 Calculation

For analyzing the effect of AR coating parameters on multijunction performance, it is useful to have a realistic numerical model for the reflectance. Here, we use the relatively simple model of Lockhart and King [23]. This model calculates the normal-incidence reflection of a three-layer coating. Each layer is assumed to be lossless so that the index of refraction  $n_j$  of the  $j$ th layer, along with its thickness  $d_j$ , fully characterizes the optical properties of the layer. The layers are numbered  $j = 1$  to 4, with  $j = 4$  being the top layer and  $j = 1$  being the substrate. For example, for a two-layer  $\text{MgF}_2/\text{ZnS}$  coat on a GaInP cell with an AlInP window layer, layers 4/3/2/1 are  $\text{MgF}_2/\text{ZnS}/\text{AlInP}/\text{GaInP}$ , respectively. The reflection  $R$  as a function of wavelength  $\lambda$  is given by

$$R = |(X - 1)/(X + 1)|^2 \quad (9.17a)$$

where

$$X = [n_2(n_3n_4 - n_2n_4t_2t_3 - n_2n_3t_2t_4 - n_3^2t_3t_4) + i n_1(n_3n_4t_2 + n_2n_4t_3 + n_2n_3t_4 - n_3^2t_2t_3t_4)]/[n_1n_4(n_2n_3 - n_3^2t_2t_3 - n_3n_4t_2t_4 - n_2n_4t_3t_4) + i n_2n_4(n_2n_3t_2 + n_3^2t_3 + n_3n_4t_4 - n_2n_4t_2t_3t_4)] \quad (9.17b)$$

and

$$t_j = \tan(2\pi n_j d_j/\lambda) \quad (9.17c)$$

Although this approach incorrectly assumes that there is no absorption from the layers of the top subcell, and completely neglects all the deeper layers in the cell stack, in practice, it gives results that agree reasonably well with more rigorous approaches [24], and it has the virtue of simplicity. The AR coating calculations that illustrate the following discussion were done using equations (9.17). Note, however, that more complex problems such as the calculation of backside AR coats needed for mechanical stacks require the more rigorous formalism.

### 9.5.8.3 Current matching

Figure 9.9(a) shows the modeled reflectance for a GaInP cell with a MgF<sub>2</sub>/ZnS AR coating, for several different combinations of the layer coating thicknesses [25], using optical constants from the literature [26, 27]. The dependence of the reflectance on the layer thicknesses can, roughly, be broken down into two parts, that is, the ratio of the two thicknesses and the total thickness of each layer. Proper choice of the ratio, as for the layer thicknesses in Figure 9.9(a), yields a reflectance with a flat, low, notch-shaped minimum. With this ratio held constant, the total thickness of the coating determines the position of the minimum, with increasing thickness shifting the notch position to lower photon energy. The width of the notch is less than the solar spectral range, so regardless of the position of the notch, the photocurrents of the subcells will be less than what they would be for the ideal case of zero reflectance. Shifting the notch to higher photon energy will send more light to the top subcell at the expense of the bottom subcell, and vice versa; the AR coating thus affects the current matching in the cell. Figure 9.9(b) shows the photocurrent of a GaInP(1.85 eV)/GaAs(1.42 eV) tandem cell as a function of ZnS/MgF<sub>2</sub> AR coating layer thicknesses, for the AM1.5 direct spectrum. As the top-subcell thickness increases, the optimal AR coating thickness increases, to compensate by directing more of the light to the bottom subcell.

## 9.5.9 Concentration

Terrestrial application of high-efficiency multijunction solar cells is generally in concentrator systems, given the high solar cell costs. These types of cells are well suited for concentrator operation, not only because of their high one-sun efficiencies, but also because these high efficiencies can be maintained up to concentration levels exceeding 1000 suns. This section discusses the adaptations needed for the one-sun devices to be made suitable for concentrator operation, and describes the resulting concentrator

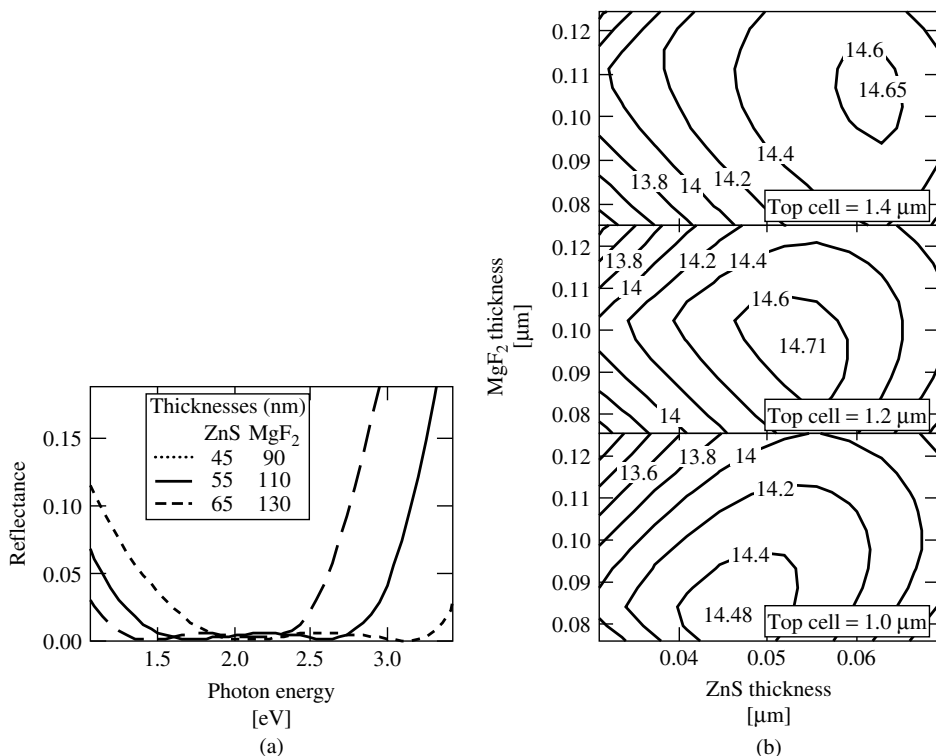


**Figure 9.9** (a) Calculated reflectance for a GaInP cell with a  $\text{MgF}_2/\text{ZnS}$  AR coating, for several different combinations of the layer coating thicknesses. (b) Calculated photocurrent (in  $\text{mA}/\text{cm}^2$ ) of a GaInP/GaAs two-terminal tandem cell under the AM1.5 direct spectrum as a function of  $\text{ZnS}/\text{MgF}_2$  AR coating layer thicknesses, for several different top-subcell thicknesses

performance to be expected from these devices. A detailed discussion of general issues in concentrator PV is given in Chapter 11 (see also Reference [28]).

### 9.5.9.1 Spectrum

Cells in a terrestrial concentrator module will be exposed to a spectrum containing significantly less high-energy light than the AM0 spectrum to which multijunction devices are exposed in space applications. This difference calls for the thickness of the terrestrial concentrator top subcell to be greater than that of a space cell, to satisfy current-matching requirements. As noted above, current-matching top-subcell thicknesses for GaInP/GaAs tandem cells are on the order of  $0.5 \mu\text{m}$  for the AM0 spectrum and  $1 \mu\text{m}$  for the AM1.5 direct spectrum. In practice, the situation is not so simple, because the spectrum that a terrestrial cell sees will vary as a function of time, and in most typical operating situations will rarely be as blue-poor as the ASTM (formerly American Soc. for Testing and Materials) standard AM1.5 direct spectrum. The cell design also depends on cell temperature, which will depend on the details of the module (and which, of course, will also vary with time). Further discussion of these issues for multijunction concentrators is given in Reference [29].

### 9.5.9.2 Concentration dependence of efficiency

Equation (9.13) shows that, for each decade of increase in  $J_{SC}$  due to a corresponding increase in the incident light flux,  $V_{OC}$  will increase by  $(kT/e) \ln(10) = 60$  mV for an ideal  $n = 1$  junction at 300 K. For a series-connected multijunction device, each junction will contribute this amount to the net increase in  $V_{OC}$  with concentration. This increase in  $V_{OC}$  gives a significant boost to cell efficiency with concentration, a boost that is relatively greater for low band gap junctions. For instance, a two-junction GaInP/GaAs cell with a one-sun  $V_{OC}$  of 2.4 V will go to  $V_{OC} = 2.76$  V at 1000 suns for an increase of 15%, whereas a three-junction GaInP/GaAs/Ge cell with a one-sun  $V_{OC}$  of 2.6 V will go to  $V_{OC} = 3.14$  V at 1000 suns for an increase of 21%. For a cell with negligible series resistance, the fill factor will also increase with concentration, although not in as numerically simple a fashion as does  $V_{OC}$ . The increase with concentration is proportionally much less than that for  $V_{OC}$ ; the fill factor typically increases on the order of 1 to 2% as the concentration is raised from 1 to 1000 suns, for the ideal case of no series resistance.

It is interesting to note that while series-connected multijunction devices maintain their current matching with increasing light intensity (assuming that the spectrum does not change), the increase in junction voltage with concentration means that voltage-matched devices are voltage-matched only for a fixed concentration ratio.

### 9.5.9.3 Series resistance and metallization

In practice, of course, series resistance is unavoidable. The resulting  $J^2R$  power loss scales as the square of the current, and thus eventually becomes a dominant factor for the cell efficiency with increasing current. This series resistance will manifest itself as a loss in the fill factor (and, at very high currents or for very high resistance, in  $J_{SC}$  as well). Series-connected multijunction cells, which distribute the spectrum into several subcells and are thus inherently lower-current devices than single-junction cells, therefore have a great advantage in minimizing  $J^2R$  losses at high concentrations. For example, the GaInP/GaAs tandem operates at half the current of a single-junction GaAs cell, and thus suffers only one quarter the  $J^2R$  loss for a given resistance and concentration.

Even with this low-current advantage of multijunction cells, in adapting a cell from one sun to concentrator operation it may be well worth reducing series resistance. One of the most vital adaptations of a cell design for concentrator operation is the front-contact metallization. The series resistance of the cell depends on the density of front-contact grid fingers [30]; a grid design optimized for 1000 suns will have a much higher density of grid fingers than a one-sun grid. Grid-finger spacings of 200  $\mu\text{m}$  or less are not unusual at 1000 suns. Naturally, decreasing the grid-finger spacing increases the device shadowing and so decreases the current; thus, concentrator grid design involves careful trade-offs of the shadowing versus the series resistance. Fortunately, with the sophisticated photolithography/evaporation/lift-off metallization processing used for high-efficiency devices, grid-finger widths on the order of 3  $\mu\text{m}$ , with height/width aspect ratios of two or more, can be achieved. Such finger dimensions allow a very dense packing of high-conductivity grids, while maintaining a reasonably low shadow loss.

An additional approach to decreasing the series resistance is to raise the emitter conductivity in the top subcell (for monolithic two-terminal devices, there is no lateral

conduction in the emitters of the other subcells, so only the top-cell emitter conductivity is important). This may be accomplished by raising the emitter doping and/or the thickness. Because doing so may decrease the quantum efficiency of the top subcell, increasing the conductivity is a trade-off that must be made carefully. Achieving a sufficiently high emitter conductivity is easier for  $n/p$  than for  $p/n$  devices, because of the higher majority-carrier mobility in  $n$ -type material than in otherwise comparable  $p$ -type material.

At least as important to the concentrator operation of monolithic two-terminal multijunction devices is the necessity for tunnel-junction interconnects (TJICs) with low series resistance, high peak tunneling currents, and low absorption losses. These considerations are discussed in more detail later in this chapter.

#### 9.5.9.4 Measured performance of GaInP/GaAs/Ge concentrator cell

The considerations of device performance versus concentration that we have just described are well illustrated by the plot of efficiency versus concentration for the GaInP/GaAs/Ge three-junction concentrator device, as shown in Figure 9.10. For concentrator operation, this device incorporated adaptations to the top-subcell emitter conductivity, the grid-finger spacing, and the top-subcell current-matching thickness. The  $V_{OC}$  of the resulting device increases with concentration at a rate quite near the ideal 60 mV/junction/decade. Because of the low one-sun current and the low series resistance, the fill factor remains virtually unaffected by series-resistance losses until several hundred suns concentration. At higher concentration, the increasingly dominant series resistance causes the efficiency to roll off. Note, however, that at 1000 suns, the efficiency is still well in excess of 30%.

#### 9.5.9.5 Linearity

In measuring the concentration dependence of device performance, it is usually assumed that  $J_{SC}$  is linear with concentration, so that  $J_{SC}$  can be used as the measure of the concentration level. The assumption of linearity is generally considered to be quite good

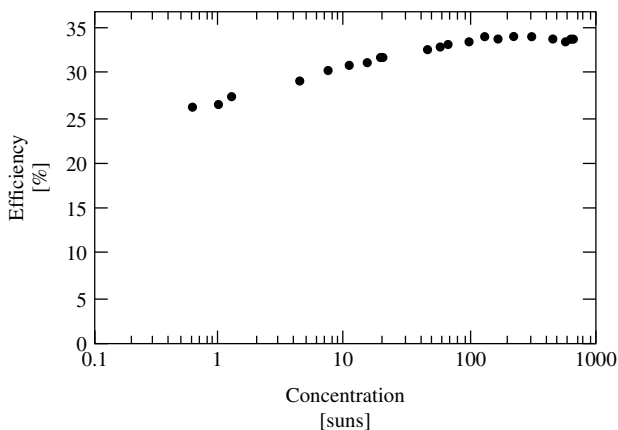


**Figure 9.10** Efficiency versus concentration of a state-of-the-art GaInP/GaAs/Ge cell under the AM1.5 global spectrum [14]

for III-V devices. Although a detailed discussion of linearity is outside the scope of this chapter, it is worth mentioning because different degrees of nonlinearity for different subcells in the device could lead to a crossover between top-cell-limited and bottom-cell-limited performance as a function of concentration.

### 9.5.10 Temperature Dependence

To predict device performance at realistic operating temperatures, and to be able to interpret measured device characteristics at these temperatures, it is useful to analyze the temperature coefficients of these devices using the basic cell equations (9.1–9.16) [31]. We shall see that the current-matching constraint for series-connected multijunction cells leads to effects in the temperature coefficients that are not seen for single-junction devices.

#### 9.5.10.1 $V_{OC}$

Because the series-connected multijunction  $V_{OC}$  is simply the sum of the subcell  $V_{OC}$ s, the temperature coefficient  $dV_{OC}/dT$  of the multijunction  $V_{OC}$  is likewise the sum of the  $dV_{OC}/dT$  values for the subcells. Taking the GaInP/GaAs tandem cell as an example, both the GaInP and GaAs subcells have  $dV_{OC}/dT \approx -2 \text{ mV}/^\circ\text{C}$ . The tandem therefore has  $dV_{OC}/dT \approx -4 \text{ mV}/^\circ\text{C}$  [31]. Table 9.2 compares these temperature coefficients for several types of cells. The GaInP/GaAs/Ge three-junction cell is seen to have a more negative  $1/V_{OC} dV_{OC}/dT$  value than the GaInP/GaAs two-junction cell, due to the contribution of the low band gap Ge junction. However, going to high concentrations reduced the magnitude of  $1/V_{OC} dV_{OC}/dT$ , due to the increase in  $V_{OC}$  with concentration.

#### 9.5.10.2 $J_{SC}$

Although the  $V_{OC}$  temperature coefficients for the subcells of a series-connected multijunction cell are independent and additive, the multijunction  $J_{SC}$  temperature coefficient

**Table 9.2**  $V_{OC}$  temperature coefficients at 300 K for multijunction cells and their single-junction component subcells, assuming junction ideality factors  $n = 1$ . One-sun illumination is assumed except as noted. Values are guidelines for comparison with actual cells, but precise agreement should not be expected, especially for junctions whose ideality factor deviates significantly from  $n = 1$ . For comparison, data are also shown for a passivated emitter rear locally diffused (PERL) Si cell, which has a significantly lower temperature coefficient than that of standard Si cells [32]

| Cell                     | $V_{OC}$<br>[mV] | $dV_{OC}/dT$<br>[mV/K] | $1/V_{OC} dV_{OC}/dT$<br>[%/K] |
|--------------------------|------------------|------------------------|--------------------------------|
| Ge                       | 200              | −1.8                   | −0.90                          |
| GaAs                     | 1050             | −2.0                   | −0.19                          |
| GaInP                    | 1350             | −2.2                   | −0.16                          |
| GaInP/GaAs               | 2400             | −4.2                   | −0.17                          |
| GaInP/GaAs/Ge            | 2600             | −6.0                   | −0.23                          |
| GaInP/GaAs/Ge (500 suns) | 3080             | −6.0                   | −0.19                          |
| PERL Si                  | 711              | −1.7                   | −0.24                          |

is more complex. Again taking the GaInP/GaAs tandem as an example, recall that GaAs subcell  $J_{SC}$  depends not only on the GaAs band gap but also on the GaInP band gap, because the GaInP subcell filters the light to the GaAs subcell. When the tandem-cell temperature is raised, the bottom-subcell band gap decreases, tending to increase its  $J_{SC}$ ; at the same time, however, the top-subcell band gap also decreases, which decreases the amount of light going to the bottom cell and thus minimizes the increase in the bottom-subcell  $J_{SC}$  with temperature.

The tandem  $J_{SC}$  is limited by the least of the subcell  $J_{SC}$ s. In general, these subcell  $J_{SC}$ s will not have identical temperature coefficients. For a tandem cell that is nearly current matched, there will, therefore be a crossover temperature below which the tandem  $J_{SC}$  is limited by one subcell and above which the tandem  $J_{SC}$  is limited by the other subcell. Figure 9.11 illustrates this crossover for a modeled GaInP/GaAs tandem

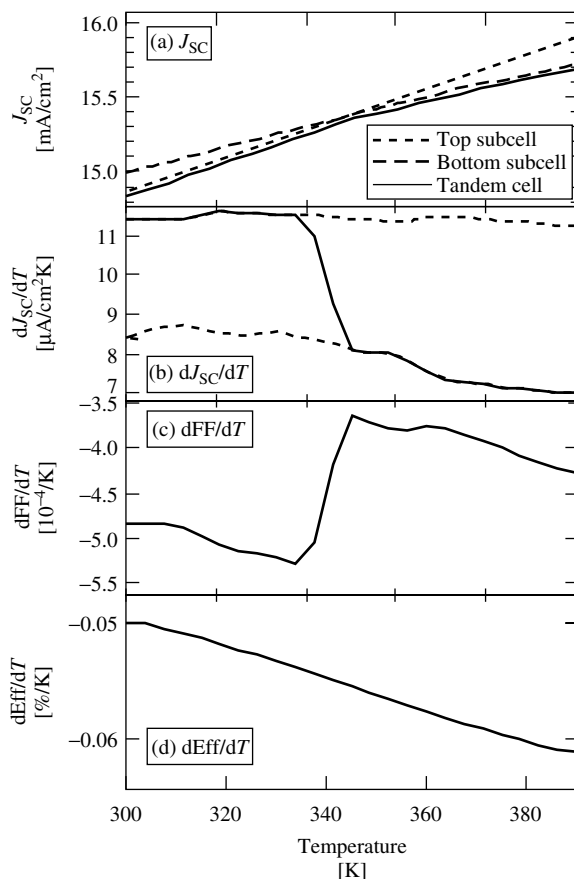


**Figure 9.11** (a) Subcell and corresponding tandem-cell  $J_{SC}$ s as a function of temperature for a GaInP/GaAs tandem cell that is slightly top-subcell current limited at 300 K. (b) The corresponding temperature derivatives  $dJ_{SC}/dT$ . As the cell temperature is raised above  $\sim 340$  K, the cell crosses over from top limited to bottom limited, and  $dJ_{SC}/dT$  changes correspondingly. (c) Tandem-cell fill factor temperature derivative  $dFF/dT$ . (d) Efficiency temperature coefficient  $dEff/dT$

cell that is slightly top-subcell limited at 300 K. The top-subcell  $J_{SC}$  increases faster with temperature than does the bottom-subcell  $J_{SC}$ , leading to a crossover from top- to bottom-subcell limited as the temperature is raised above 350 K. The tandem  $dJ_{SC}/dT$  likewise crosses over from  $dJ_{SCt}/dT$  to  $dJ_{SCb}/dT$ .

#### 9.5.10.3 Fill factor

Because the tandem-cell fill factor is determined more by the current-limiting subcell than by the other subcell(s), the current-matching crossover has similar implications for  $dFF/dT$  as for  $dJ_{SC}/dT$ . For the cell of Figure 9.11, the crossover from top- to bottom-subcell limited causes  $dFF/dT$  to change, as shown in Panel (c).

#### 9.5.10.4 Efficiency

Because the efficiency is proportional to  $V_{OC} \times J_{SC} \times FF$ , and  $dJ_{SC}/dT$  and  $dFF/dT$  change in opposite directions as the temperature goes through the current-matched temperature,  $dEff/dT$  is a relatively smooth function of temperature.

## 9.6 MATERIALS ISSUES RELATED TO GaInP/GaAs/Ge SOLAR CELLS

### 9.6.1 Overview

In the previous section, we discussed the basic elements of a monolithic, multijunction solar cell, such as that shown in Figure 9.1, including subcell band gaps and thicknesses, metallization, and AR coating effects. We also assumed unity collection efficiency for all photogenerated carriers, implying that component semiconductor materials, interfaces, and junctions are virtually perfect. In practice, however, numerous intrinsic and extrinsic factors tend to limit the quality and performance of multijunction solar cells. In this section, we review various aspects of real materials and devices, including issues associated with their growth.

### 9.6.2 MOCVD

The GaInP/GaAs/Ge dual- and triple-junction solar cells are produced commercially in relatively large volumes by several companies in the United States. These cells are fabricated in large MOCVD reactors made by Emcore Corporation in the United States and Aixtron in Germany. Although these devices can be grown by other techniques such as molecular beam epitaxy (MBE) [33], the predominant growth technique is MOCVD and is, therefore, the focus of this section. A description of the basic MOCVD reactors used at NREL can be found elsewhere [34]. Briefly, most of the results presented here are from layers and devices grown by MOCVD using trimethylgallium (TMG), trimethylindium (TMI), arsine, and phosphine in a Pd-purified  $H_2$  carrier gas. The dopants sources included  $H_2Se$ ,  $Si_2H_6$ , diethylzinc (DEZ), and  $CCl_4$ .



## 9.6.3 GaInP Solar Cells

### 9.6.3.1 Lattice matching

One of the major advantages of the monolithic GaInP/GaAs/Ge solar cell is that it is composed of semiconductors that are all closely lattice matched. The fabrication of such a monolithic structure is achieved by the generic process of heteroepitaxy, the specific process being MOCVD. Close lattice matching makes the job of heteroepitaxy much easier, especially for chemically similar materials such as AlGaAs on GaAs. The heteroepitaxy of lattice-mismatched materials is generally more difficult. The lattice mismatch is accommodated by nucleation and by propagation of dislocations in concentrations that depend on the amount of mismatch and the thickness of the individual layers. These dislocations are often centers for nonradiative recombination, in effect limiting the minority-carrier lifetime or diffusion length, and ultimately the efficiency of the device.

The lattice constant of the semiconductor alloy  $\text{Ga}_x\text{In}_{1-x}\text{P}$  is linearly related to the composition  $x$  by

$$a_{\text{Ga}_x\text{In}_{1-x}\text{P}} = xa_{\text{GaP}} + (1 - x)a_{\text{InP}} \quad (9.18)$$

where  $a_{\text{GaP}} = 0.54512$  nm and  $a_{\text{InP}} = 0.58686$  nm are the lattice constants of GaP and InP, respectively (see Table 9.3). An epitaxial layer of  $\text{Ga}_x\text{In}_{1-x}\text{P}$  on GaAs with  $a_{\text{GaAs}} = 0.565318$  nm will be lattice matched to GaAs at  $25^\circ\text{C}$  for  $x = 0.516 = x_{\text{LM}}$ . The quality of a thin, epitaxial  $\text{Ga}_x\text{In}_{1-x}\text{P}$  layer is relatively good for small variations of  $x$  around  $x_{\text{LM}}$ . This case is shown in Figure 9.12, in which a broad-spectrum photocurrent from an electrolyte/ $\text{Ga}_x\text{In}_{1-x}\text{P}$  junction is plotted as a function of  $\Delta\theta$  (see Section 9.7.1). The quantity  $\Delta\theta$  is measured by double-crystal X-ray rocking-curve diffraction and is a measure of  $x$  [35]. If the thickness of the  $\text{Ga}_x\text{In}_{1-x}\text{P}$  layer is less than the  $x$ -dependent critical thickness, then

$$\Delta\theta = \tan\theta_{\text{B}} \left( \frac{xa_{\text{GaP}} + (1 - x)a_{\text{InP}} - a_{\text{GaAs}}}{a_{\text{GaAs}}} \right) \left( \frac{1 + [\nu_{\text{GaP}}x + \nu_{\text{InP}}(1 - x)]}{1 - [\nu_{\text{GaP}}x + \nu_{\text{InP}}(1 - x)]} \right) \quad (9.19)$$

**Table 9.3** Lattice constants, force constants, and Poisson ratios for selected III-V binary compounds. Values from Reference [37]

| Material   | Lattice constant<br>[nm] | $C_{11}$<br>[ $10^{10}$ N/m $^2$ ] | $C_{12}$<br>[ $10^{10}$ N/m $^2$ ] | Poisson ratio, $\nu$ |
|--|--------------------------|------------------------------------|------------------------------------|----------------------|
| AlP  | 0.546354                 |                                    |                                    |                      |
| GaP  | 0.54512                  | 14.12                              | 6.25                               | 0.307                |
|  |                          | 14.05                              | 6.203                              | 0.306                |
| InP  | 0.58686                  | 10.22                              | 5.76                               | 0.360                |
| InP  |                          | 10.11                              | 5.61                               | 0.357                |
| $\text{Ga}_x\text{In}_{1-x}\text{P}$ [ $x = 0.516$ ] |                          |                                    |                                    | 0.333                |
| GaAs   | 0.565318                 | 11.81                              | 5.32                               | 0.311                |
|  |                          | 11.91                              | 5.951                              | 0.333                |
| InAs   | 0.60583                  | 8.329                              | 4.526                              | 0.352                |
| Ge   | 0.5657906                | 12.89                              | 4.83                               | 0.273                |
|  |                          | 12.40                              | 4.13                               | 0.250                |

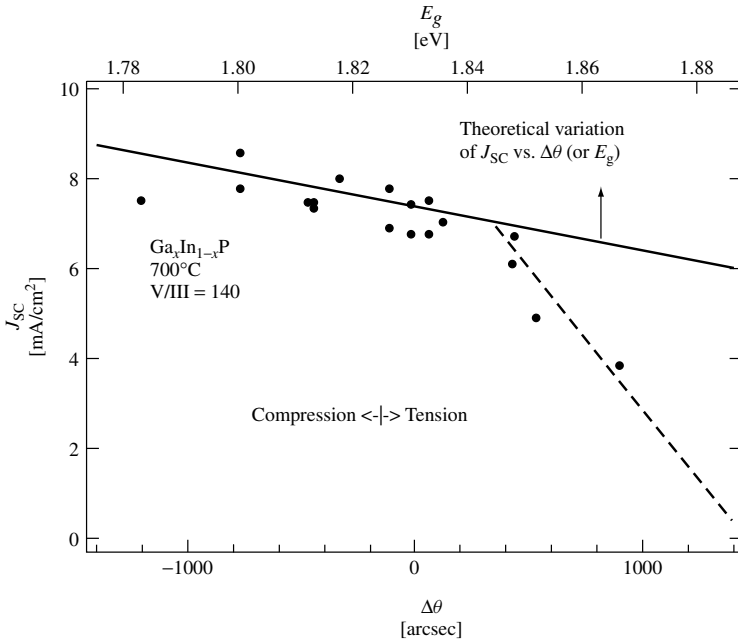


**Figure 9.12** Saturated photoelectrochemical current density of Ga<sub>x</sub>In<sub>1-x</sub>P as a function of the lattice mismatch as measured by X-ray rocking-curve peak separation in units of arc seconds, or equivalently as a function of the resulting  $E_g$  [35]. The growth temperature is 700°C and V/III ratio (PH<sub>3</sub>/(TMGa + TMIIn)) is 140. The dashed line is included to guide the eye

where  $\theta_B$  is the Bragg angle and  $\nu_{GaP}x + \nu_{InP}(1 - x)$  is the Poisson ratio for Ga<sub>x</sub>In<sub>1-x</sub>P obtained from Poisson ratios for GaP and InP (see Table 9.3). (The Poisson ratio is defined as the negative of the ratio of the lateral to the longitudinal strains under uniaxial stress.) If the epilayer is fully relaxed, the last multiplicative term of equation (9.19) goes to one. A plot of  $\Delta\theta$  versus  $x$  for Ga<sub>x</sub>In<sub>1-x</sub>P on GaAs for these two extremes is shown in Figure 9.13(a). The critical layer thickness is simply the balance between the coherent energy created by strain, the relief of this strain energy by the introduction of dislocations, and the self-energy of dislocations. Below the critical layer thickness, the lowest-energy state of the system is an epilayer with a lattice constant, in the plane of the interface between the epilayer and the substrate, equal to the lattice constant of the substrate. Above the critical epilayer thickness, the lowest-energy state is one composed of some epilayer strain and some strain-relieving dislocations. The problem was first solved by Matthews and Blakeslee [36]. The relationship between lattice mismatch and layer thickness is shown in Figure 9.13(b).

Referring to Figure 9.12, for  $\Delta\theta = 0$ , the critical layer thickness is infinite and  $J_{SC}$  is a measure of the intrinsic minority-carrier transport quality of the epilayer in the absence of misfit dislocations. The solid line with negative slope is the theoretical variation of  $J_{SC}$  with  $\Delta\theta$ . For  $\Delta\theta < 0$ , the epilayer is In-rich ( $x < x_{LM}$ ), and its band gap is lower than that of lattice-matched Ga<sub>x</sub>In<sub>1-x</sub>P. Hence,  $J_{SC}$  increases with decreasing  $\Delta\theta$ . For  $\Delta\theta > 0$ , the epilayer is Ga-rich ( $x > x_{LM}$ ). At first,  $J_{SC}$  decreases with increasing  $\Delta\theta$  in line with the In-rich portion of the curve, but then falls off rapidly with increasing  $\Delta\theta$ . The critical

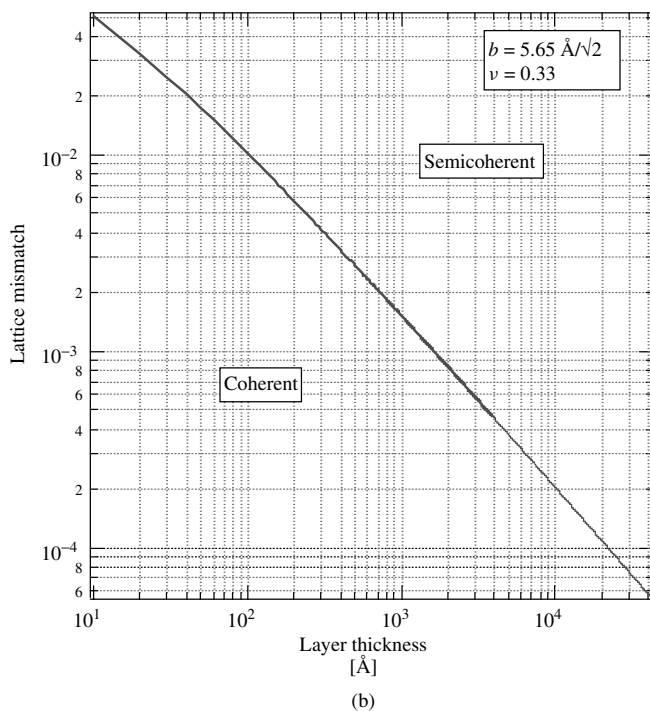
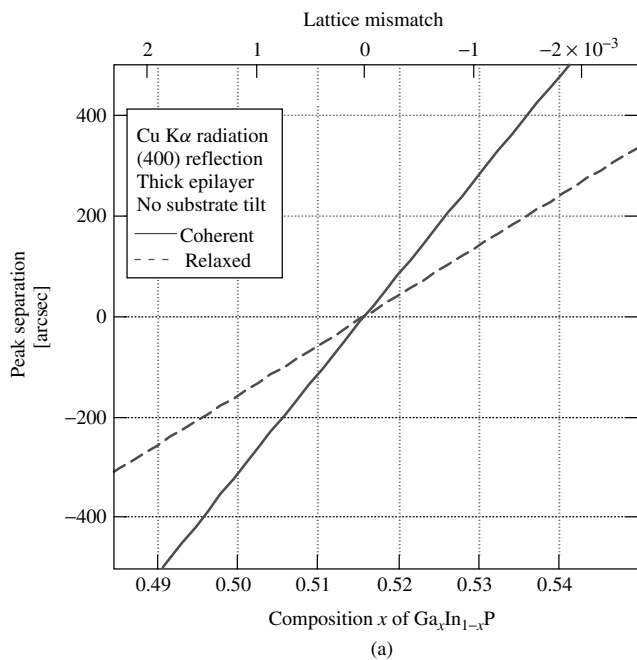


**Figure 9.13** (a) A plot of  $\Delta\theta$  versus  $x$  for  $\text{Ga}_x\text{In}_{1-x}\text{P}$  on GaAs; (b) Critical misfit versus layer thickness

$\Delta\theta$  at which this occurs is a function of kinetic factors including the layer thickness, growth temperature, and growth rate. Experimentally, the critical  $\Delta\theta$  also depends on the sign of  $\Delta\theta$  as can be seen in Figure 9.12. Indium-rich material is under compression. It is generally more difficult (and takes longer) to generate misfit and threading dislocations in compressively strained material compared to material under tension; hence, the difference in strain-relaxation behavior. Intuitively, the critical layer thickness for compressively strained material will generally approach that of tensively strained material as the growth temperature is increased and/or the growth rate is decreased. This behavior is relatively common. Note that this is contrary to the theoretical calculation shown in Figure 9.13(b). This calculation considers only the equilibrium state of the epilayer; the sign of the strain is, therefore, immaterial.

The thickness of the  $\text{Ga}_x\text{In}_{1-x}\text{P}$  top cell for most conditions will be on the order of 1  $\mu\text{m}$  or less. From Figure 9.13(b) this would imply that the critical lattice mismatch should be less than  $2 \times 10^{-4}$  or  $|\Delta\theta| \leq 50$  arcsecond. There are several factors that tend to increase or decrease this tolerance limit such as the following:

- Material lattice matched at room temperature is lattice mismatched at growth temperature. This is due to a difference in the thermal expansion coefficients between  $\text{Ga}_x\text{In}_{1-x}\text{P}$  and GaAs (see Table 9.4). For kinetic reasons, it is probably more important that the layers are lattice matched at growth temperature. A layer that is lattice matched at a growth temperature of 625°C will exhibit a lattice mismatch of  $\Delta\theta \sim -200$  arcsecond at room temperature [38], or alternatively, a layer that is lattice matched at room temperature, would exhibit a  $\Delta\theta = 200$  arcsecond at 625°C. Because it is easier to introduce misfit dislocations at high temperatures, it is probably better to grow the layer lattice matched at the growth temperature. Hence, a  $\pm 50$  arcsecond tolerance at growth temperature would yield a room temperature tolerance of  $-250 < \Delta\theta < -150$  arcsecond.

**Table 9.4** Important properties of Ge, GaAs, and GaInP at 298 K

|   | Ge  | GaAs                       | $\text{Ga}_x\text{In}_{1-x}\text{P}$   | $\text{Al}_x\text{In}_{1-x}\text{P}$    |
|---|---|----------------------------|--|---|
| Atoms/ $\text{cm}^3$  | $4.42 \times 10^{22}$                     | $4.44 \times 10^{22}$      |  |   |
| Lattice constant [ $\text{\AA}$ ]                           | 5.657906 [37]                             | 5.65318 [37]               | $= a_{\text{GaAs}}$ for<br>$x = 0.516$ | $= a_{\text{GaAs}}$ for<br>$x = 0.532$  |
| Energy gap [eV]   | Indirect<br>0.662<br>Direct<br>0.803 [37] | 1.424 [37]                 | Disordered<br>1.91 [41]                | Indirect<br>2.34<br>Direct<br>2.53 [37] |
| Density of states   |   |                            |  |   |
| Conduction band<br>$N_C$ [ $\text{cm}^{-3}$ ]               | $1.04 \times 10^{19}$                     | $4.7 \times 10^{17}$       |  |   |
| Valence band<br>$N_V$ [ $\text{cm}^{-3}$ ]                  | $6.0 \times 10^{18}$                      | $7.0 \times 10^{18}$       |  |   |
| Intrinsic carrier concentration [ $\text{cm}^{-3}$ ]        | $2.33 \times 10^{13}$                     | $2.1 \times 10^6$          |  |   |
| Linear coefficient of thermal expansion [ $\text{K}^{-1}$ ] | $7.0 \times 10^{-6}$ [37]                 | $6.0 \times 10^{-6}$ [37]  | $5.3 \times 10^{-6}$ [38]              |   |
|   |   | $6.63 \times 10^{-6}$ [38] |  |   |

- As mentioned above, material grown under compression is usually more stable to relaxation than material under tension, allowing one to err more toward negative values of  $\Delta\theta$ .
- Because of dynamical scattering effects, the measured  $\Delta\theta$  for a thin ( $\leq 0.1 \mu\text{m}$ ) epilayer will be less than that of a thicker layer with the same composition and lattice mismatch [39].
- The value of  $\Delta\theta$  for epilayers grown on nonsingular (100) substrates is not unique, but depends on the orientation of the substrate with respect to the X-ray beam. The effective  $\Delta\theta$  is the average of two measurements of  $\Delta\theta$ . The first measurement is made in the conventional manner; the second measurement is made with the sample rotated by  $180^\circ$  [40]. For vicinal substrates close to (100), this effect is small, usually  $\sim 10\%$  at misorientation of  $6^\circ$ ; however, for {511} substrates, the effect is closer to 50%.

### 9.6.3.2 Optical properties of GaInP

#### 9.6.3.2.1 Ordering in GaInP

Prior to 1986, it was generally assumed that the band gap of a III-V ternary alloy semiconductor such as  $\text{Ga}_x\text{In}_{1-x}\text{P}$  was a unique function of the composition, and most publications showed  $\text{Ga}_x\text{In}_{1-x}\text{P}$ , lattice matched to GaAs, as having a band gap of 1.9 eV. However, in 1986 Gomyo *et al.* [42] reported that the band gap of  $\text{Ga}_x\text{In}_{1-x}\text{P}$  grown by MOCVD was usually less than 1.9 eV and depended on the growth conditions. In a subsequent paper [43], they showed that the band gap shift was correlated with the ordering of Ga and In on the Group III sublattice. The ordered structure is CuPt-like, with alternating {111} planes of  $\text{Ga}_{0.5+\eta/2}\text{In}_{0.5-\eta/2}\text{P}$  and  $\text{Ga}_{0.5-\eta/2}\text{In}_{0.5+\eta/2}\text{P}$ , where  $\eta$  is the long-range order parameter. Perfectly ordered GaInP ( $\eta = 1$ ) would be composed of alternating {111} planes of GaP and InP. The first theoretical treatments of ordering in  $\text{Ga}_x\text{In}_{1-x}\text{P}$  were put forward by Kondow and coworkers [44] using the tight binding theory, and by Kurimoto and Hamada [45] using the “first-principles” Linearized Augmented Plane Wave (LAPW) theory.

The functional relationship between the band gap’s change,  $\Delta E_g$ , and the order parameter for GaInP was first published by Capaz and Koiller [46]:

$$\Delta E_g = -130\eta^2 + 30\eta^4 \text{ (in meV)} \quad (9.20)$$

A more recent result [47] suggests that

$$\Delta E_g = -484.5\eta^2 + 435.4\eta^4 - 174.4\eta^6 \text{ (in meV)} \quad (9.21)$$

The effects of various growth parameters on the ordering and the band gap of  $\text{Ga}_x\text{In}_{1-x}\text{P}$  have been studied extensively. The band gap of  $\text{Ga}_x\text{In}_{1-x}\text{P}$  is a function not only of the growth temperature,  $T_g$ , but also of the growth rate,  $R_g$ , the phosphine partial pressure,  $P_{\text{PH}_3}$ , substrate misorientation from (100), and the doping level. Some of these effects are illustrated in Figure 9.14. Although the behavior is very complicated, there are a few characteristics that stand out. For example, for substrates that are closely oriented to within a few degrees of (100), the band gap of GaInP, using typical values for  $T_g$ ,  $R_g$ , and

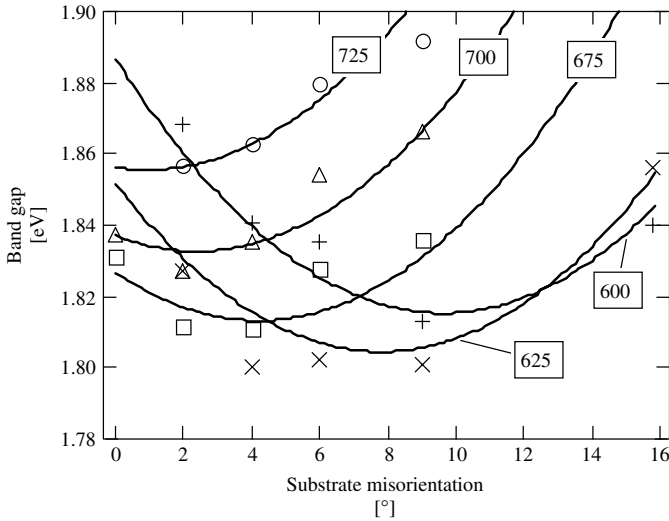


**Figure 9.14** Band gap of  $\text{Ga}_x\text{In}_{1-x}\text{P}$  versus  $T_g$  (from 600 to 725°C) and substrate misorientation

$P_{\text{PH}_3}$ , is closer to 1.8 eV than 1.9 eV. One can obtain band gaps closer to 1.9 eV using extreme values for  $T_g$ ,  $R_g$  or  $P_{\text{PH}_3}$ , but the material typically suffers in some other way, for example, minority-carrier diffusion length, composition, or morphology. The most straightforward way to obtain higher band gaps is by using substrates that are strongly misoriented from (100) toward {111}. The {111} surface in the zinc blende system is the Group III terminated surface and is often referred to as (111)A. Substrates misoriented towards (111)B generally enhance the degree of ordering. When growing on Ge there is no distinction between A and B misoriented substrates, and it is typically very difficult to control the A/B character of the III-V (GaAs or GaInP) epilayer. Hence, the easiest way to obtain high band gap GaInP on Ge is to use misorientation angles larger than about 15°, coupled with high  $R_g$ , moderate  $T_g$ , and low  $P_{\text{PH}_3}$ .

There are other material properties that are affected by ordering, including optical anisotropy [48–51], transport anisotropy [52, 53], and surface morphology [54, 55].

#### 9.6.3.2.2 Absorption coefficient

For modeling and characterization of GaInP epilayers and solar cells, accurate models for the optical properties of GaInP are required. The optical constants of GaInP have been measured by using spectroscopic ellipsometry and modeled by several groups [56, 57] and by using transmission measurements by Kurtz *et al.* [10]. These results are summarized in Figure 9.15. For the most part, there is no single model that adequately describes the broadband optical properties of lattice-matched GaInP with some arbitrary degree of ordering. The model of Kato [57] appears adequate for short wavelengths but fails for near-gap optical properties. The models of Schubert and Kurtz only account for near band gap transitions. The model of Kurtz *et al.* for the absorption coefficient is given by:

$$\alpha = 5.5\sqrt{E - E_g} + 1.5\sqrt{E - (E_g + \Delta_{\text{so}})}[\mu\text{m}^{-1}] \quad (9.22)$$

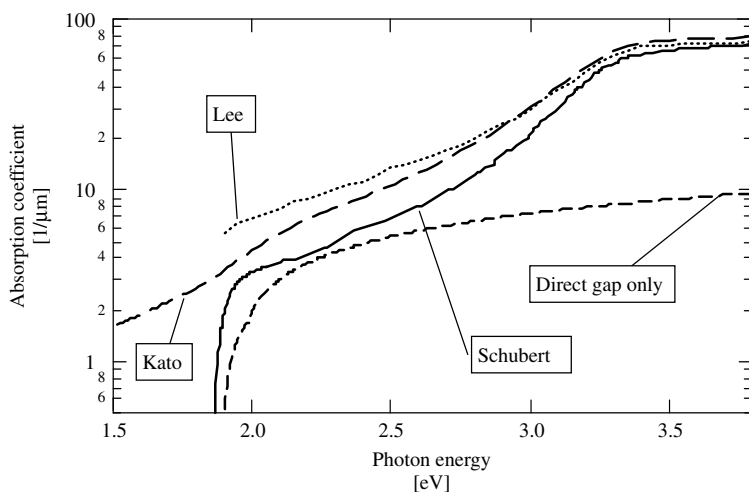


**Figure 9.15** Comparison of absorption coefficients of  $\text{Ga}_x\text{In}_{1-x}\text{P}$  published in the literature. The data of Lee *et al.* [59] and Schubert *et al.* [56] are ellipsometric data. The model of Kato *et al.* [57] is a reasonably good fit at high energies, but is a poor fit for sub-band gap photon energies. The curve marked “direct gap only” is a plot of equation (9.22)

where the photon energy  $E$ , the band gap energy  $E_g$ , and the spin orbit energy  $\Delta_{\text{so}}$  are in units of eV. The value of  $E_g$ , of course, varies with the degree of order,  $\eta$ , and the value of  $\Delta_{\text{so}}$  is typically set to 0.1 eV, independent of  $\eta$ . This model reasonably accounts for the absorption associated with the two near-band transitions at  $E_g$  and  $E_g + \Delta_{\text{so}}$  and is useful for deducing the minority-carrier diffusion length from near-gap photoresponse measurements [58]. It is not a good model for adsorption at higher photon energies.

### 9.6.3.3 Doping characteristics

#### 9.6.3.3.1 *n*-type dopants

##### Selenium

The element Se is a commonly used *n*-type dopant in III-V materials and is usually obtained from the decomposition of  $\text{H}_2\text{Se}$ . The doping behavior of  $\text{H}_2\text{Se}$  has been studied by a number of investigators [60–65]. Under most growth conditions, the electron concentration increases with  $\text{H}_2\text{Se}$  flux or partial pressure and then saturates at about  $2 \times 10^{19}/\text{cm}^3$ , depending on  $T_g$ . The incorporation of Se also depends on the partial pressure of  $\text{PH}_3$  (for GaInP) or  $\text{AsH}_3$  (for GaAs). These data best fit an equation of the form

$$n^{-1} = (1 + \alpha P_V)(\beta P_{\text{Se}})^{-1} + k^{-1} \quad (9.23)$$

where  $n$  is the electron concentration and  $P_V$  and  $P_{\text{Se}}$  are Group V and Se partial pressures, respectively. The coefficients  $\alpha$  and  $\beta$  depend on  $T_g$  and carrier flow rate (residence time) and, therefore, must be determined for each reactor system. This doping behavior can be derived from a modified Langmuir adsorption model that accounts for the competitive absorption of Se and the Group V species on a fixed number of sites,  $k$ , which will depend,

for example, on the density of steps and kinks, that is, the substrate misorientation. This model is a much better fit than the *ad hoc* form  $n \propto P_{\text{Se}}^x P_{\text{V}}^y$  most often published in the literature.

For electron concentrations greater than about  $2 \times 10^{18}/\text{cm}^3$ , the band gap energy of GaInP increases, the ordering decreases, and the morphology of the growth surface becomes very smooth [63]. At sufficiently high fluxes of Se, the surface again begins to roughen. At the same time, the electron concentration begins to decrease [60] and Se precipitates are observed in Transmission Electron Microscopy (TEM) [1]. Selenium has been linked to DX-like centers in  $(\text{Al}_x\text{Ga}_{1-x})_{0.5}\text{In}_{0.5}\text{P}$  with Al concentrations greater than about  $x = 0.4$  [66].

## Silicon

Silicon is another widely used dopant in III-V materials and devices and the most popular source is  $\text{Si}_2\text{H}_6$ . The first report of using  $\text{Si}_2\text{H}_6$  to dope GaInP was by Hotta and coworkers [67]. They found that for  $T_g < 640^\circ\text{C}$ ,  $n$  decreased with decreasing  $T_g$  presumably due to a decrease in  $\text{Si}_2\text{H}_6$  pyrolysis rate. For  $T_g > 640^\circ\text{C}$ ,  $n$  saturates at about  $n = 5 \times 10^{18}/\text{cm}^3$  with  $\text{Si}_2\text{H}_6$ , presumably due to the formation of nonionized complexes, such as  $(\text{Si}_{\text{III}}^+ - \text{Si}_{\text{V}}^-)$  or  $(\text{Si}_{\text{III}}^+ - \text{V}_{\text{III}}^-)$ . The results [67] for Si-doped GaAs were quantitatively similar. Scheffer and coworkers [68] saw no evidence of saturation for electron concentrations up to  $8 \times 10^{18}/\text{cm}^3$  using  $\text{Si}_2\text{H}_6$ , whereas Minagawa and coworkers [69] found that the electron concentration saturated at about  $1 \times 10^{19}/\text{cm}^3$ , essentially independent of substrate orientation and growth temperature.

It has been shown that Si delta doping (where the doping is confined to a single layer or series of layers) in GaInP increases the maximum electron concentration and increases the electron mobility relative to that of uniformly doped layers [70, 71]. The conclusion from these studies is that Si delta doping yields fewer Si shallow acceptor defects. Silicon apparently does not introduce any deep states in GaInP, but does so in  $(\text{Al}_x\text{Ga}_{1-x})_{0.5}\text{In}_{0.5}\text{P}$  for  $x > 0.3$  [72]. As with Se, Si concentrations above some critical level tend to disorder  $\text{Ga}_x\text{In}_{1-x}\text{P}$ , causing the band gap to increase. However, the details can be quite varied. Gomyo and coworkers [62] reported that a lower concentration of Si than that for Se was required to disorder GaInP. However, Minagawa and coworkers [69] found that Si concentrations closer to  $1 \times 10^{19}/\text{cm}^3$ , depending on  $T_g$ , were required to dissolve the ordering in  $\text{Ga}_x\text{In}_{1-x}\text{P}$ .

### 9.6.3.3.2 *p*-type dopants

## Zinc

The most common *p*-type dopant in GaInP is Zn. The typical sources are dimethylzinc (DMZ) and diethylzinc (DEZ). The Zn doping characteristics have been studied by a number of investigators [35, 60, 61, 73]. The incorporation efficiency is typically sublinear with the input flow, and increases with lower growth temperature and higher growth rate  $R_g$ . A model that accounts for some of these effects has been proposed by Kurtz *et al.* [73].

High Zn concentrations cause several problems in GaInP. Carrier concentrations in the neighborhood of  $1 \times 10^{18}/\text{cm}^3$  destroy the ordering in  $\text{Ga}_x\text{In}_{1-x}\text{P}$  and increase the



band gap [74]. And high Zn concentrations (or more accurately, high DEZ flows) cause a loss of In from both GaInP [35] and AlGaInP [75]. The problem is probably associated with some parasitic gas-phase reaction involving DEZ, TMIIn, and PH<sub>3</sub>. The effect can be large enough to measurably change the growth rate and the Ga/In ratio in the material. The Ga/In ratio can be so far from lattice-matched conditions as to affect the morphology. High DEZ flows also inhibit the incorporation of Ga, but to a lesser extent.

Diffusion of zinc during epilayer growth can cause degradation of the performance of solar cells [76]. The zinc dopant in the substrate, back-surface field (BSF), or tunnel-junction layers can serve as a reservoir for zinc diffusion into the base region of an *n*-on-*p* cell. The diffusion is largely driven by point defects that are injected during the growth of the *n*-type layers. The diffusion can be reduced by reducing the doping levels of any of the layers (including the *n*-type layers), by adding diffusion barriers, and/or by using Se instead of Si doping of the *n*-type layers [76]. A side effect of the Zn diffusion is a disordering of any of the ordered structures [77].

The effect of changing the cap or overlying layer and cooling atmosphere on the hole concentration in Zn-doped (Ga<sub>1-x</sub>Al<sub>x</sub>)<sub>0.5</sub>In<sub>0.5</sub>P,  $x = 0.7$ , has been studied by Minagawa and coworkers [78]. Cooling in a H<sub>2</sub> atmosphere containing AsH<sub>3</sub> or PH<sub>3</sub> reduces the hole concentration. Hydrogen radicals from the decomposition of Group V hydrides easily diffuse into the epilayers and passivate the Zn acceptors. Cap layers of *n*- or *p*-GaAs help impede the indiffusion of H, and underlying layers can enhance the indiffusion of H, a special problem with *p*-on-*n* cells [76].

## Magnesium

Magnesium doping (with cyclopentadienyl magnesium) in AlGaInP has been studied by a number of investigators [74, 79–82]. It is useful for achieving higher hole concentrations in AlGaInP and AlInP layers. However, the Mg incorporation efficiency decreases with decreasing temperature. Therefore, higher growth temperatures are favored, which is an advantage for AlGaInP. However, since dopant diffusion rates increase rapidly with temperature, this is a disadvantage for the fabrication of stable tunnel junctions and stable GaAs/Ge interfaces. For GaInP, it has no obvious advantages over Zn, and suffers from rather severe memory effects [80]. Also, relatively good-quality Zn-doped AlInP can be obtained by paying careful attention to source material and system purity [83].

## Carbon

The use of C (from CCl<sub>4</sub> or CBr<sub>4</sub>) has not been studied extensively. The halide tends to etch GaInP [84], indium more so than gallium. Also, C-doped GaInP exhibits poor minority-carrier transport properties [84, 85].

### 9.6.3.4 Window layers and back-surface fields

#### 9.6.3.4.1 AlInP window layers

The function of an emitter window layer is to passivate the surface states associated with the emitter surface. These states are minority-carrier traps. Their effect is characterized by a quantity called the surface (or interface) recombination velocity, *S*. The value of *S*

can range from  $10^7$  cm/s for an unpassivated GaInP emitter to less than  $10^3$  cm/s for a high-quality AlInP/GaInP interface. A high interface recombination velocity will reduce the photoresponse of the GaInP solar cell, most strongly in the blue portion of the spectral response. To be an effective window layer for an  $n$ -on- $p$  cell, the material should have a

- lattice constant close to that of GaInP,
- $E_g$  much larger than that of the emitter,
- large valence-band offset with respect to the emitter to provide a potential barrier for minority holes,
- relatively high electron concentration (on the order of  $n \geq 18/\text{cm}^3$ ), and
- material quality sufficient to produce low-interface recombination velocity.

The semiconductor AlInP has most of the required characteristics.  $\text{Al}_x\text{In}_{1-x}\text{P}$  is lattice matched to GaAs for  $x = 0.532$ . The indirect band edge of AlInP is 2.34 eV, 0.4 to 0.5 eV larger than that of GaInP. The  $\text{Al}_x\text{In}_{1-x}\text{P}/\text{GaInP}$  band alignment appears to be Type 1 with  $\Delta E_c \sim 0.75\Delta E_g$  and  $\Delta E_v \sim 0.25\Delta E_g$  [86]. This implies that it should provide reasonable confinement of the holes in the emitter of an  $n$ -on- $p$  device. It is easily doped  $n$ -type with either Si or Se. The internal quantum efficiency of a GaInP cell with a good  $\text{Al}_x\text{In}_{1-x}\text{P}$  window layer is greater than about 40% at a photon energy of 3.5 eV. However, there is a strong affinity between the Al in  $\text{Al}_x\text{In}_{1-x}\text{P}$  and oxygen, and oxygen is a deep donor in  $\text{Al}_x\text{In}_{1-x}\text{P}$ . Hence, if the reactor chamber or the source materials are contaminated with water vapor or other oxygenated compounds, the quality of the  $\text{Al}_x\text{In}_{1-x}\text{P}$  will suffer. Poor-quality  $\text{Al}_x\text{In}_{1-x}\text{P}$  will degrade the blue response of a GaInP cell and degrade the fill factor (via contact resistance) [8].

#### 9.6.3.4.2 Back-surface barrier

The function of the top-cell back-surface barrier is to passivate the interface between the top-cell base and the tunnel-junction interconnect (TJIC). Also, in some cases, it may help reduce outdiffusion of dopants from the TJIC [87]. The high recombination velocity at this interface will affect both the photoresponse (in particular, the red photoresponse) and the  $V_{OC}$ . The  $V_{OC}$  effect is shown in Figure 9.8. Note that the magnitude of the effect can be quite large and is also affected by the base minority-carrier diffusion length and thickness. The requirements of a good back-surface barrier layer are similar to those of a front-surface window layer. For an  $n$ -on- $p$  cell, it should have a

- lattice constant close to that of GaInP,
- $E_g$  larger than  $E_g$  of GaInP,
- large conduction-band offset with respect to GaInP,
- relatively high hole concentration (on the order of  $p = 1 \times 10^{18}/\text{cm}^3$ ),
- relatively good minority-carrier transport properties, and
- high transparency to photons destined for the underlying GaAs cell.

For back-surface fields, initial results from Friedman *et al.* [88] implied that disordered or high- $E_g$  GaInP was the best BSF for a low- $E_g$  GaInP top cell compared to an AlGaInP BSF. This was probably due to oxygen contamination in the AlGaInP layer.

As a deep donor, oxygen is a bigger problem in  $p$ -type AlGaInP. Other researchers found that strained, Ga-rich  $\text{Ga}_x\text{In}_{1-x}\text{P}$  was superior to either disordered lattice-matched GaInP or AlGaAs [89]. Recently, however, the best commercial tandem solar cells use AlGaInP [90] or AlInP [91] BSFs. The growth of high-quality Zn-doped AlInGaP and the techniques for assessing the quality thereof have been published by several others [81, 83, 92].

### 9.6.3.5 Characteristics of state-of-the-art GaInP cells

Because the band gap of GaInP can change so dramatically with growth conditions, it is not meaningful to talk of “state-of-the-art” GaInP cells using only efficiency as the measure of quality. As the band gap increases,  $V_{OC}$  should increase, but  $J_{SC}$  and efficiency should decrease. (Note, however, that the efficiency of a current-matched GaInP/GaAs tandem cell should increase slightly with increasing GaInP band gap as discussed in Section 9.5.4 above.) Also, in any optimized multijunction solar cell the thickness of the GaInP cell is likely to be optically thin, that is, it will absorb fewer photons and hence *may* be lower in efficiency than an optically thick cell. So thickness and band gap are two important parameters that must be considered when comparing single-junction efficiencies. In general, relative measures of quality, for example,  $V_{OC}/E_g$ , are more useful.

## 9.6.4 GaAs Cells

### 9.6.4.1 Quality of GaAs on Ge(100) substrates

Despite the close lattice matching between GaAs and Ge substrates, the quality of GaAs grown on Ge can be quite variable. (See Section 9.6.5.3 for a discussion on the heteroepitaxy of GaAs on Ge.) The primary criterion for good-quality heteroepitaxial GaAs is, of course, the efficiency of overlying GaAs and GaInP solar cells. Generally, a good indicator of quality is a specular episurface with little or no haze (often caused by antiphase domains or APDs) and few extended defect features such as pits, hillocks, or slip lines. For a specular, epitaxial GaAs layer, one should observe a faint “crosshatch” pattern. This “crosshatch” is a replica or shadow of the misfit dislocation array located in the GaAs/Ge interface plane. Sometimes, the absence of this “crosshatch” pattern is an indicator that the misfit is being relaxed by threading dislocations. The density of these threading dislocations can become high enough to affect the minority-carrier transport properties of the GaAs and GaInP solar cells, and should, therefore, be avoided.

The morphology of  $\text{Ga}_x\text{In}_{1-x}\text{P}$  grown on GaAs is an even more sensitive indicator of the quality of the original GaAs surface. Morphologically faint defects in or on the GaAs will be “decorated” by the growth of  $\text{Ga}_x\text{In}_{1-x}\text{P}$ . This is probably caused by differences in the attachment of Ga and In to the different surface orientations offered by the defect.

GaAs grown on Ge can be “lattice matched” to the Ge substrate by the addition of about 1% indium. This eliminates the “crosshatch” in good heteroepitaxy, but does not appear to make the task of heteroepitaxy any easier. Under the best conditions, a  $\text{Ga}_{0.99}\text{In}_{0.01}\text{As}$  solar cell will be slightly better than a GaAs cell on Ge [93].

### 9.6.4.2 Optical properties

The optical parameters of GaAs are tabulated in the work of Aspnes and coworkers [94] and a model for the optical dielectric function of GaAs (and  $\text{Al}_x\text{Ga}_{1-x}\text{As}$ ) has been proposed [95].

### 9.6.4.3 Window layers and back-surface fields

$\text{Ga}_x\text{In}_{1-x}\text{P}$  and  $\text{Al}_x\text{In}_{1-x}\text{P}$  should both make excellent window layers and back-surface field layers for GaAs solar cells [96, 97]. Both have Type 1 band alignment with GaAs, with reasonably adequate conduction- and valence-band offsets [86, 98]. Ideally,  $\text{Al}_x\text{In}_{1-x}\text{P}$  would make a better window layer than  $\text{Ga}_x\text{In}_{1-x}\text{P}$  because of its larger band gap energy. However, because of its sensitivity to oxygen contamination,  $\text{Al}_x\text{In}_{1-x}\text{P}$  will probably never produce as good an interface with GaAs as does  $\text{Ga}_x\text{In}_{1-x}\text{P}$ . (This is the main problem with the  $\text{AlGaAs/GaAs}$  interface used widely for single-junction GaAs solar cells [19].) The undoped  $\text{Ga}_x\text{In}_{1-x}\text{P/GaAs}$  interface has one of the lowest interface recombination velocities ( $S < 1.5 \text{ cm/s}$ ) of any heterostructure ever measured, including the  $\text{SiO}_2/\text{Si}$  interface [96]. In addition, it is difficult to dope  $\text{Al}_x\text{In}_{1-x}\text{P}$   $p$ -type at a level of  $p > 1 \times 10^{18}/\text{cm}^3$ . For these reasons,  $\text{Ga}_x\text{In}_{1-x}\text{P}$  is usually the preferred window layer and BSF layer for GaAs solar cells in  $\text{GaInP/GaAs}$  tandem-cell structures.

## 9.6.5 Ge Cells

### 9.6.5.1 Optical properties of Ge

The optical and electronic properties of Ge are well documented (see Reference [37]). Germanium has a lattice constant close to that of GaAs and has a diamond structure. It is also mechanically stronger than GaAs and, hence, has long been viewed as an excellent substitute for GaAs substrates. With a band gap of 0.67 eV, it is current matched to a thin GaAs top cell [7] and is also a good bottom-cell candidate in a four-junction stack [99]. However, in both these cases, it has several properties that put it at a disadvantage:

- The  $V_{OC}$  is limited by its indirect band gap to about 300 mV and is relatively more sensitive to temperature [100].
- It is relatively expensive, hence, it cannot be viewed as a one-sun solar cell material (with the exception of its use in space).
- Germanium is an  $n$ -type dopant in GaAs and GaInP. In GaInP, it also exhibits amphoteric behavior with a compensation ratio  $N_a/N_d = 0.4$  [101] and has been associated with a deep acceptor state [102].
- Gallium, As, In, and P are all shallow dopants in Ge. Hence, the control of the junction-formation process becomes complicated when it is combined with the III-V heteroepitaxy process (*vide infra*).

### 9.6.5.2 Junction formation

Diffusion of a Group V or a Group III dopant into a Ge substrate is the most common junction-formation process for Ge subcells. Indeed, because of the proximity of III-V

epilayers and the high temperatures involved in heteroepitaxial process, diffusion of both Group III and Group V atoms into the Ge substrate is unavoidable. The challenge is to control the process so as to obtain a Ge subcell with good photovoltaic properties and simultaneously form a defect-free heteroepitaxial layer of GaAs with the appropriate conductivity type and level. A detailed description of the optimum process is beyond the scope of the review, but a few critical factors that have to be considered are listed below:

- Diffusion coefficients are thermally activated. So, in general, dopants and junctions are less mobile and more stable at lower growth temperatures.
- As noted by Tobin *et al.* [103], the diffusion coefficient of As in Ge at 700°C is higher than that of Ga, but the solid solubility of Ga is larger than that of As.
- For three-junction GaInP/GaAs/Ge devices with a reasonably good-quality Ge subcell, the only Ge device parameter that is of consequence is the  $V_{OC}$ , because the  $J_{SC}$  of the Ge subcell is potentially much greater than that of the GaInP (or GaAs) subcell.
- The highest  $V_{OC}$  of a Ge solar cell reported to date is 0.239 [100]. This  $V_{OC}$  is a sensitive function of process conditions and is most sensitive to the quality of the III-V/Ge interface and its fabrication [100].
- AsH<sub>3</sub> etches Ge. The etch rate increases with temperature and AsH<sub>3</sub> partial pressure. Heavily etched, singular and vicinal Ge(100) surfaces are microscopically rough [104]. Hence, prolonged AsH<sub>3</sub> exposures should be avoided.
- The etch rate for PH<sub>3</sub> is much lower, and there appears to be much less roughening of the surface from PH<sub>3</sub> exposure [104]. The diffusion coefficient of P at 600°C is about two orders of magnitude lower than that of As [37]. Hence, PH<sub>3</sub> may be a better Group V, *n*-type dopant than AsH<sub>3</sub>.

### 9.6.5.3 III-V heteroepitaxy

Although there are a number of “recipes” for the growth of GaAs on Ge(100) with specular morphologies or low antiphase domain (APD) or low stacking-fault densities, many present contradictory results. For example, Pelosi *et al.* [105] found that the GaAs surface morphology is best for very low V/III ratio (on the order of 1), using a moderate growth rate ( $R_g \sim 3.5 \mu\text{m/h}$ ) and a low growth temperature ( $T_g = 600^\circ\text{C}$ ). On the other hand, Li *et al.* [106] found that the lowest APD density occurs for high V/III, low  $R_g$ , and high  $T_g$ . Chen *et al.* [107] showed that “good” morphology could only be obtained for growth temperatures in the range of 600°C to 630°C.

The cause for this striking difference is not known with certainty. It may be due to differences in reactor design or purity. It may be related to the quality of the Ge substrates. Other researches [104] would suggest that it is related to the prenucleation conditions or the state of the Ge surface immediately prior to the GaAs nucleation step.

A lot has been published about the structure of Ge(100), but most of it is with regard to surfaces prepared in ultrahigh-vacuum (UHV) or MBE environments. It has been shown, however, that under most conditions, AsH<sub>3</sub>-treated surfaces in an MOCVD reactor are quite different as explained below [104, 108, 109]. Arsenic on a Ge(100) terrace forms rows of dimers, similar to As on GaAs(100) [108, 109]. This reduces the  $(1 \times 1)$  symmetry of the unreconstructed Ge surface to a surface that now has a  $(2 \times 1)$

or a  $(1 \times 2)$  surface symmetry. For the  $(2 \times 1)$  reconstruction, the dimer bonds are parallel and rows of dimers run perpendicular to the step edges. Adjacent terraces on an (100) As-terminated Ge surface can be composed of orthogonal reconstructions; adjacent terraces on a (100) GaAs are always of the same type. An As-terminated Ge surface prepared in a UHV or MBE environment usually exhibits a single-domain,  $(1 \times 2)$  symmetry. An MOCVD-prepared surface will initially be  $(1 \times 2)$ , but tends toward  $(2 \times 1)$  symmetry with a transition time that ranges from one minute to tens of minutes and that depends on temperature,  $\text{AsH}_3$  partial pressure, and substrate temperature. Intermediate states, of course, are composed of a mixture of  $(1 \times 2)$  and  $(2 \times 1)$  domains, a condition that is conducive to the formation of APDs in a GaAs heterolayer. Also, as mentioned above,  $\text{AsH}_3$  etches Ge. This etching causes significant step bunching or faceting and microscopically rough surfaces.

### 9.6.6 Tunnel-junction Interconnects

The purpose of the tunnel-junction interconnect between the GaInP and GaAs subcells is to provide a low-resistance connection between the  $p$ -type BSF of the GaInP cell and the  $n$ -type window layer of the GaAs bottom cell. Without the TJIC, this  $p$ - $n$  junction has a polarity or forward turn-on voltage that is in opposition to that of the top or bottom cells and, when illuminated, would produce a photovoltage that could roughly negate the photovoltage generated by the top cell. A tunnel junction is simply a  $p^{++}n^{++}$  junction where  $p^{++}$  and  $n^{++}$  represent heavily or degenerately doped material. The space charge region for a  $p^{++}n^{++}$  junction should be very narrow,  $\sim 10$  nm. In forward bias, the normal thermal current characteristic of a  $p$ - $n$  junction is “shorted” by tunneling through the narrow space charge region. Hence, the forward IV characteristic of a tunnel junction behaves much like a resistor for current densities less than some critical value, called the peak tunneling current,  $J_p$ . The functional form of  $J_p$  is dominated by an exponential term of the form:

$$J_p \propto \exp\left(-\frac{E_g^{3/2}}{\sqrt{N^*}}\right) \quad (9.24)$$

where  $E_g$  is the band gap and  $N^* = N_A N_D / (N_A + N_D)$  is the effective doping concentration [110]. The value of  $J_p$  must be larger than the photocurrent of the tandem cell. For a concentrator cell operating at 1000 suns,  $J_{SC} \sim 14$  A/cm<sup>2</sup>. If  $J_p < J_{SC}$ , the behavior of the tunnel junction current switches to that dominated by the usual thermionic emission and the voltage drop across the tunnel junction increases to that of a typical  $p$ - $n$  junction.

The best tunnel junctions for very high efficiency solar cells are relatively defect-free. Lifetime limiting, midgap defects usually only add to the excess current. There is no evidence in the literature that point or extended defects add to  $J_p$  or increase the conductivity in the tunneling portion of the  $I$ - $V$  curve. High excess currents can mask a low  $J_p$ , but usually the junction conductivity is also unacceptably low. On the other hand, it is possible that high concentrations of point or extended defects can compensate donors or acceptors in the junction leading to increased depletion width and lower tunneling currents. In addition, defects can reduce the thermal stability of the tunnel junction and the quality of the overlying layers. Therefore, in general, it is usually best to grow the TJICs free of point or extended defects.

The first high-efficiency GaInP/GaAs dual-junction solar cells were fabricated using an optically thin GaAs TJIC. The best tunnel junctions were doped with C and Se. Hence, they were reasonably stable under the thermal conditions required to grow the top cell and were capable of operating at more than 1000 suns, that is,  $J_p > 14 \text{ A/cm}^2$ . They were also less than 30 nm thick and obscured less than 3% of the light destined for the lower cell. With optically thick, unannealed devices, peak tunneling currents were greater than  $300 \text{ A/cm}^2$  with excess current densities close to zero [8].

#### 9.6.6.1 AlGaAs/GaInP TJIC

Despite the higher band gap and its concomitant penalty, the  $p^{++}\text{-AlGaAs}/n^{++}\text{-GaInP}$  heterojunction tunnel diode proposed by Jung and coworkers is the preferred TJIC for one-sun operations and may be suitable for concentration [111]. It takes advantage of the innate propensity for AlGaAs to incorporate C and for GaInP to incorporate Se, so that high values of  $N^*$  are easily achieved. Hence, peak tunneling currents as high as  $80 \text{ A/cm}^2$  were reported. The devices are also thermally stable;  $J_p$  is reduced to about  $70 \text{ A/cm}^2$  for 30-min anneal at  $650^\circ\text{C}$  and to about  $30 \text{ A/cm}^2$  for a 30-min anneal at  $750^\circ\text{C}$ . This TJIC is more optically transparent than a thin GaAs TJIC and therefore should yield a higher tandem-cell photocurrent.

### 9.6.7 Chemical Etchants

The processing of epitaxial products into finished devices is beyond the scope of this chapter. Most of the processes used by the industry are proprietary, and there are numerous laboratory processes, such as evaporation of metals and optical coatings, that are suitable for research. One very useful area that is common to both industrial and laboratory processes is the use of selective and nonselective etchants for the various materials used in GaInP/GaAs multijunction solar cells. A list of these etchants is given below (etch rates are at room temperature). Note that solutions containing  $\text{H}_2\text{O}_2$  typically exhibit an etch rate that depends on the age of the solution [112].

- Mixtures of ammonia, hydrogen peroxide, and water etch GaAs, but do not etch GaInP and AlInP. A common formulation is 2 parts  $\text{NH}_4\text{OH}$ , 1 part 30%  $\text{H}_2\text{O}_2$ , and 10 parts  $\text{H}_2\text{O}$  (2:1:10). Also, a solution of  $\text{H}_3\text{PO}_4$ ,  $\text{H}_2\text{O}_2$ , and  $\text{H}_2\text{O}$  combined in a ratio of 3:4:1 etches GaAs and not GaInP.
- Concentrated HCl rapidly etches GaInP, but the surface is easily passivated by dilute HCl and HCl vapor. HCl does not etch GaAs.
- Dilute HCl: $\text{H}_2\text{O}$  etches AlInP [113].
- Au metallization is impervious to both 2:1:10 and concentrated HCl.
- A 1:20 solution of HCl and  $\text{CH}_3\text{COOH}$  (acetic acid) etches GaInP at a rate of  $70 \text{ nm/min}$  and GaAs at a rate of  $<5 \text{ }\mu\text{m/min}$  [112].
- $5\text{H}_2\text{SO}_4:1\text{H}_2\text{O}_2:1\text{H}_2\text{O}$  at room temperature etches GaInP at a rate of about  $25 \text{ nm/min}$ . It etches GaAs much more rapidly ( $>1 \text{ }\mu\text{m/min}$ ).
- Mixtures of HCl: $\text{H}_3\text{PO}_4$ : $\text{H}_2\text{O}$  etch GaInP [114]. For high HCl compositions, the etch rate is  $\sim 1 \text{ }\mu\text{m/min}$ .

### 9.6.8 Materials Availability

A question of interest for all solar cell technologies is the availability of the component materials required for very large scale, long-term production of the cell. Predicting the long-term availability of such natural resources as gallium, indium and germanium is very difficult. This issue has been studied periodically over the years, including a recent thorough work by Andersson [115]. It appears that the material whose availability constrains production for the GaInP/GaAs/Ge structure may prove to be germanium. If so, one approach would be to forfeit the relatively small additional contribution of the Ge third junction by using the two-junction GaInP/GaAs structure grown on GaAs. Also, reuse of the substrate by liftoff of the active junctions may prove practical. In any case, high-concentration operation of these cells makes the best use of their constituent materials.

## 9.7 TROUBLESHOOTING

The standard procedures for measuring light and dark  $I$ - $V$  curves and  $QE$  curves are described in Chapter 16. Here, we describe additional techniques for characterizing materials and devices. The symptoms of common problems are tabulated in Table 9.5.

### 9.7.1 Characterization of Epilayers

When working with alloys like GaInP, rocking-mode X-ray diffraction is very helpful toward confirming that the desired lattice constant (alloy composition) was realized (see above).

A modified Polaron profiler (available from Bio Rad) can measure the carrier concentration, band gap, and minority-carrier diffusion length of an epilayer [58, 116]. The sample is mounted in a special holder that allows the formation of front and back contacts in a fraction of the time that is required by a typical solid-state device. An ohmic contact is made to the back of the wafer by passing a surge of current (something like a spot weld). A junction is formed between the epilayer and an aqueous electrolyte (e.g. 0.1 M HCl). The capacitance-voltage ( $C$ - $V$ ) characteristics of this junction provide a measure of the carrier concentration as a function of depth. In a finished device, the carrier concentrations of the individual layers can be checked by profiling (etching) through the structure in the electrochemical cell, or by using selective etches to uncover the layer(s) of interest.  $C$ - $V$  measurements on a processed single-junction device (rather than on an aqueous-semiconductor junction) tend to give lower dissipation factors because of lower series resistance, but only give information about the lightly doped side of the junction. Thus, it can be difficult to ascertain whether the emitter is underdoped by a  $C$ - $V$  profile on the solid-state device. Although a Polaron profiler is designed to measure the doping level of each layer as a multilayered stack is etched, etch profiles of a multijunction solar cell require considerable skill and some luck. Nonuniform etching can distort the results, especially if the material has some defects. Also, some layers may be completely depleted. Often, a Polaron profiler gives the best information when the etching is partly done by the profiler and partly by applying selective etches *ex situ*. (See Section 9.6.7.) A (dilute) mixture of ammonia and hydrogen peroxide etches GaAs, but stops at GaInP and AlInP,



**Table 9.5** Troubleshooting for *n-on-p* cells

| Problem                                  | Symptom  | Confirmation   |
|--|--|--|
| Window too thick                         | Poor blue response   | Model <i>QE</i>  |
| High front-surface recombination         | Poor blue response (lower $V_{OC}$ )                       | Model <i>QE</i>  |
| $L_{emitter} < \text{emitter thickness}$ | Poor blue response (lower $V_{OC}$ )                       | Model <i>QE</i>  |
| Emitter doping too high                  | Poor blue response (low $V_{OC}$ , low emitter sheet res.) | Measure doping of emitter  |
| Emitter doping too low                   | Low $V_{OC}$ ; higher emitter sheet resistance             | Depleted emitter   |
| Base doping too low                      | Low $V_{OC}$   | Measure doping of base   |
| Base doping too high                     | Low $V_{OC}$ ; reduced red response                        | Dark <i>I-V</i> likely to have $n = 1$                                     |
| $L_{base} < \text{base thickness}$       | Low $V_{OC}$ ; reduced red response                        | Dark <i>I-V</i> likely to have $n = 1$                                     |
| High back-surface recombination          | Low $V_{OC}$ (reduced red response)                        | Dark <i>I-V</i> likely to have $n = 1$                                     |
| Threading dislocations                   | Low $V_{OC}$ (low FF and $J_{SC}$ )                        | High dark current, probably with $n = 2$                                   |
| Thin metallization                       | Low FF – series resistance                                 | Measure grid-line resistance   |
| Bad tunnel junction                      | Low FF – series resistance and/or low $V_{OC}$             | Measure tunnel junction by itself  |
| Extra junction                           | Low FF – (nonohmic?) series resistance                     | Shape of <i>I-V</i> may depend on spectrum                                 |
| Metallization does not make good contact | Low FF – (nonohmic?) series resistance                     | Use transmission line on front; two pads on back                           |
| Resistive window layer                   | Low FF – series resistance                                 | Use transmission line to measure resistance to emitter                     |
| Particulate                              | Low FF – shunt   | Light emitted in forward bias may be correlated with morphological defects |
| Incomplete mesa isolation                | Low FF – shunt, sometimes with unphysically high $J_{SC}$  | Etch mesas deeper or cleave edges  |
| Front metal touches lower layer          | Low FF – shunt   | Examine under microscope   |
| Severe chromatic aberrations             | Low FF for cell measured under concentration               | Shape of <i>I-V</i> is unusual [22]  |

whereas concentrated HCl etches GaInP and AlInP, but not GaAs. GaInP does not always etch in concentrated HCl, especially if the surface is wet, the HCl is not full strength, and/or if the GaInP surface has previously been in contact with a dilute HCl solution.

A window is provided in the Polaron cell for shining light on the aqueous semiconductor junction. The photocurrent (*QE*) from the junction can fit the form

$$QE = \alpha(h\nu)^*L/[1 + \alpha(h\nu)^*L] \quad (9.25)$$

where  $h\nu$  is the photon energy, and it is assumed that  $L$  is much longer than the depletion width but less than the layer thickness.

The fit value for  $L$  will reflect the minority-carrier diffusion length when  $L$  is greater than the depletion width, but less than the thickness of the layer. For small  $\alpha(h\nu)^*L$ , the  $QE$  is proportional to  $\alpha(h\nu)$ , allowing an easy fit to determine  $E_g$  from  $\alpha(h\nu) = A^*(h\nu - E_g)^{0.5}$ .

Photoluminescence (PL) intensity is commonly used to test the quality of a material, but the intensity strongly depends on carrier concentration and surface recombination. Time-resolved PL measurements on double heterostructures (passivated layers) of different thicknesses can quantify both the minority-carrier lifetime and the interface recombination velocity [117, 118].

### 9.7.2 Transmission Line Measurements

Once a device is made, in addition to the  $I$ - $V$  and  $QE$  measurements, characterization of the device contacts using a transmission line measurement is useful toward diagnosing problems. Transmission lines [119] allow determination of the contact resistance ( $\rho_c$ ) and the sheet resistance ( $R_s$ ). The resistance,  $R$ , between any two pads as a function of  $x$ , the distance between the pads, is estimated by:

$$R = 2\rho_c/(w^2) + R_s/w^*x \quad (9.26)$$

where  $w$  is the width of the transmission line and the dimension of the square pads.  $\rho_c$  and  $R_s$  are calculated from the intercept and slope of the line [119]. If the sheet resistance is large compared with the contact resistance, then the current across the semiconductor/pad interface is not uniform, and the estimated  $\rho_c$  can be refined to a more accurate value of the contact resistance,  $\rho'_c$ , using the equation:

$$\rho'_c = \rho_c^2/(w^2 R_s)^* \tanh^2\{w^2 R_s/[\rho_c^* \tanh(w^2 R_s/\rho_c)]\} \quad (9.27)$$

### 9.7.3 $I$ - $V$ Measurements of Multijunction Cells

The chapter on measurements (Chapter 16) describes how to measure the light  $I$ - $V$  curve for a standard reference spectrum and for systematically varied spectra. Complete diagnosis of a multijunction cell requires characterization (an  $I$ - $V$  curve) of each of the active junctions to quantify their photocurrents and shunting. It would also be useful to establish the photovoltages and series resistances of each junction, but these are difficult or impossible for a two-terminal, series-connected cell. We describe here some alternative approaches for characterizing the individual junctions.

In some situations, it is possible to apply a contact between the series-connected junctions. The three-terminal configuration allows measurement of each junction of a two-junction cell. For a three-junction cell, a three-terminal measurement allows independent measurement of the top or bottom cells, but measurement of the middle cell by itself may require four connections. A primary advantage of the three-terminal approach is that it allows measurement of the photovoltage of each junction. The measured photocurrents should be adjusted for the change in junction area that occurred when the third connection

was applied. Also, the increased perimeter area of the top cell sometimes affects the dark current.

Underlying junctions may be investigated by first chemically removing the upper junctions. In this case, the underlying junction will respond to a wider spectral range.

It is also useful to be able to characterize two-terminal multijunction cells. The shape of the  $I$ - $V$  curve of a series-connected multijunction cell is dominated by the characteristics of the junction that generates the smallest photocurrent. (This concept can be understood by reviewing Figure 9.5 above.) The  $I$ - $V$  curve for each junction can be measured by adjusting the spectrum so that that junction has the smallest photocurrent. Using these measurements, the estimated individual junction  $I$ - $V$  curves can be derived mathematically, as described in Reference [120]. An example is given below. From the individual  $I$ - $V$  curves, one can calculate the  $I$ - $V$  curve for the multijunction cell under an arbitrary spectrum. For some samples, the  $J_{SC}$  values may be measured by reverse biasing the cell beyond the breakdown points of the junctions [121].

#### 9.7.4 Evaluation of Morphological Defects

Careful examination of the devices with a microscope can identify many problems, especially when the device is forward biased so that it emits light, or when an optical beam-induced current (OBIC) image is available. GaInP junctions emit red light that is usually visible to the naked eye. GaAs emission may be observed with an infrared (IR) imaging device. If the emission shows dark or bright spots, these can usually be correlated with a morphological defect, giving an explanation to the problem. Also, metal (e.g. a contact pad) that extends to the very edge of the pad may touch a layer that is nearby and short the device. This failure mode can sometimes be detected by microscopic examination.

#### 9.7.5 Device Diagnosis

In general, a low  $J_{SC}$  may be evaluated from the energy dependence of the photocurrent loss. It is useful to measure and model the internal  $QE$ . The external  $QE$  measurements are described in Chapter 16. The internal  $QE$  is modeled according to equations (9.2–9.8) (Figure 9.16) and is determined experimentally from

$$QE_{\text{Internal}} = QE_{\text{external}} / (1 - \text{Reflectivity}) \quad (9.28)$$

Accurate knowledge of the absorption coefficient is essential to successfully model the  $QE$ . The absorption coefficients of GaAs and GaInP were discussed above.

Figure 9.17(a) compares the  $QE$  of a typical GaInP cell  $QE$  (solid line) with what would be expected if there were no loss in the AlInP window (top curve) or a poor collection in the emitter (bottom curves). Although window absorption losses can easily be distinguished from emitter losses, the similarity of the two lower curves demonstrate the difficulty of distinguishing poor front-surface recombination from poor emitter material quality. However, it is somewhat easier to differentiate poor base material quality from poor rear passivation using a series of devices with variable base thickness. A cell with a

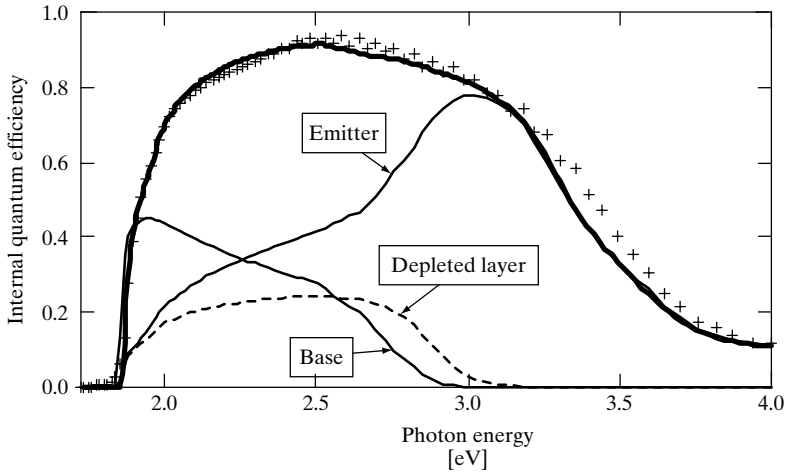


**Figure 9.16** Measured (crosses) and modeled (lines) quantum efficiency of a GaInP solar cell. The contributions from the different layers of the solar cell are labeled and demonstrate how the emitter dominates the blue response, whereas the base dominates the red response

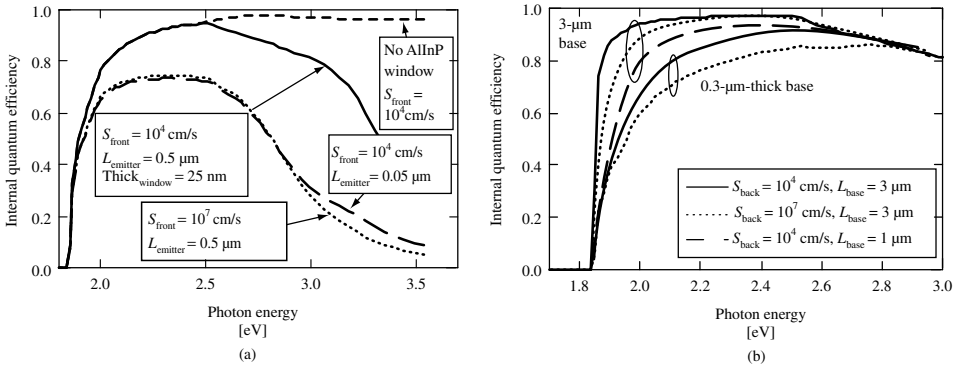


**Figure 9.17** Modeled *QE* of GaInP cell. (a) The solid line, relative to the “no AlInP window” line, shows the effect of absorption of 25 nm of AlInP. The two lower curves show the degradation from an increased front-surface recombination velocity ( $S_{\text{front}}$ ) or from a decreased emitter diffusion length ( $L_{\text{emitter}}$ ). (b) Compares a thin and a thick GaInP cell

thick base layer is more sensitive to the diffusion length in the base, whereas a cell with a thin base layer is relatively more sensitive to the quality of the back-surface field (see Figure 9.17(b)).

There are numerous reasons why the  $V_{\text{OC}}$  or FF may be degraded. Table 9.5 enumerates many of these, and Figure 9.18(a) illustrates one example.

Extra junctions are more likely to be problems when working with Ge because III-V elements dope Ge and Ge dopes the III-V materials. The back of the Ge wafer must be etched before processing to avoid an extra junction at the back [100]. Accidental junctions in Ge are often highly shunted, with nearly ohmic  $I$ - $V$  characteristics. In this case, these

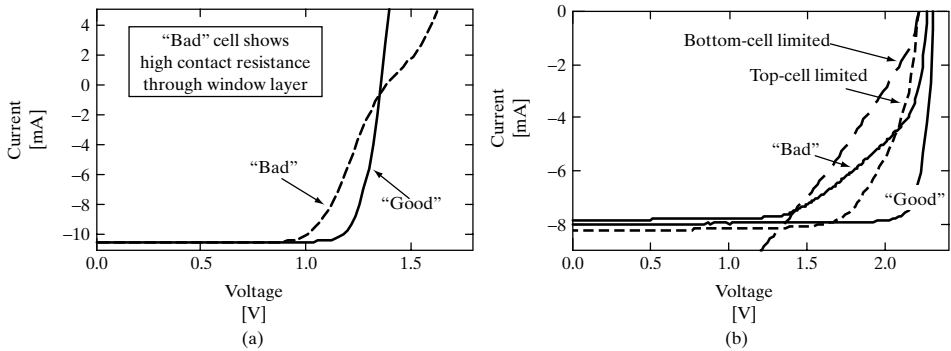


**Figure 9.18** (a) Comparison of  $I$ - $V$  curves for a "good" GaInP cell and a GaInP cell with an extra junction caused by the AlInP window. Transmission line measurements showed that the contact resistance was high through the window layer. (b)  $I$ - $V$  curves for good and bad GaInP/GaAs tandem cells. The "bad" curve shows a shunt; measurements of the same cell under bottom-cell limited and top-cell limited conditions show that the shunt is in the bottom junction

are easiest to observe at high concentration because the  $V_{OC}$  of the Ge junction increases faster with the photocurrent than that of the intended junction. Spurious junctions in the Ge may add, subtract, or do both (in the case of back-to-back junctions) to the  $V_{OC}$ .

When a two-junction cell shows evidence of shunting, it is useful to determine which of the two junctions is shunted. This can be determined by measuring the light  $I$ - $V$  curve under two different spectra, one of which reduces the photocurrent of the top junction, and the other which reduces the photocurrent of the bottom junction [120]. The example in Figure 9.18(b) shows a case in which the bottom cell is shunted. This sort of problem is often related to defects originating from particulate or poor wafer quality. Particulate exposure before or during growth is often a bigger problem for GaInP/GaAs cells than for single-junction cells.

## 9.8 FUTURE-GENERATION SOLAR CELLS

The GaInP/GaAs/Ge cell is close to maturity for space applications, but the efficiencies being reported by the manufacturers are continuing to increase, with champion cells measuring near 30% AM0 efficiency [122]. The efficiency reported by Spectrolab for a terrestrial concentrator version of the GaInP/GaAs/Ge solar cell [14, 123] is likely to improve. The theoretical efficiency is 45% at 500 suns under the AM1.5 global spectrum. Historically, III-V based multijunction cells have achieved 80% to 90% of their theoretical efficiencies [99].

### 9.8.1 Refinements to the GaInP/GaAs/Ge Cell

An improvement in the AM0 efficiency of the GaInP/GaAs/Ge cell is predicted when the GaInP band gap is increased. However, addition of aluminum to the GaInP cell has been shown to increase the band gap, but not the efficiency, of the top cell because the  $J_{SC}$  was reduced by more than 10% while the  $V_{OC}$  increased only slightly, if at all,

presumably because of the adverse effect of Al (and the associated oxygen contamination) on minority-carrier properties [122].

The Ge junction collects about twice as much photocurrent as the other two junctions in the GaInP/GaAs/Ge cell. The three-junction cell efficiency will increase, theoretically, if the GaAs band gap is lowered, the Ge band gap is increased, or a fourth junction is added between the GaAs and Ge junctions.

The most common approach is to add indium to the GaAs layer and perhaps to the GaInP layer. A small amount of indium improves the lattice matching to Ge and improves the efficiency of the cell even without the use of any buffer layer [124]. Addition of larger quantities of indium (e.g. 12%) is being widely investigated in the hope of increasing the efficiency by  $\sim 2\%$  absolute [125]. Higher efficiencies require the growth of a buffer layer that successfully relieves the strain without allowing threading (and other) dislocations to propagate into the active layers of the solar cell. Results are promising, but the efficiencies, so far, have been similar to those for lattice-matched cells [125–128]. Researchers at Varian studied a two-step approach allowing the mismatched layers to be grown on the back of the wafer, whereas the “sunny-side” layers were grown lattice matched [129, 130]. The effects of lattice mismatch on the manufacturability and lifetime of solar cells are not known.

Considerable effort has also been invested toward the addition of a fourth, 1-eV junction (to be added between the GaAs and Ge junctions). Such a four-junction structure has a theoretical efficiency of  $>50\%$  [99], translating to a practical efficiency of 40% if appropriate materials could be identified. Unfortunately, identifying an appropriate (high quality and lattice matched to GaAs) 1-eV material has proven difficult. The most promising candidate for this junction is currently the alloy GaInAsN. Other materials have been investigated, but do not show as much promise. ZnGeAs<sub>2</sub> is somewhat difficult to grow (especially at low pressures) and can cause cross contamination (e.g. Zn contamination of subsequent growth) [131]. Ga<sub>0.5</sub>Tl<sub>0.5</sub>P was reported to be lattice matched to GaAs with a band gap of about 0.9 eV [132], but a number of laboratories have been unable to duplicate the original report [133, 134]. The band gap of BGaInAs lattice matched to GaAs has been pushed down to 1.35 eV, but so far, not to 1.0 eV [135]. BGaInAs also exhibits inferior material quality [136], resulting in devices with decreased photovoltages and currents.

Ga<sub>1-x</sub>In<sub>x</sub>As<sub>1-y</sub>N<sub>y</sub> can be grown lattice matched ( $x = 3y$ ) to GaAs with a band gap of about 1 eV [137], but the minority-carrier diffusion length is small [138–140]. GaAsN is unusual because the band gap decreases from 1.4 eV to about 1 eV with the addition of about 3% nitrogen. The alloy scattering is expected to be larger than in a conventional alloy, partially explaining the reduced majority-carrier mobility. However, the more serious problem is the low minority-carrier lifetimes, which have not yet been adequately explained. C and H contamination of MOCVD-grown GaInAsN is reported to be higher than that for MBE-grown GaInAsN [141], but the MBE material has not been evaluated for solar cells.

## 9.8.2 Mechanical Stacks

A high-efficiency result may also be obtained by a mechanical stack, relaxing the need to consider lattice matching. The most probable candidates for this are GaInP/GaAs stacked

over either GaInAsP (1 eV)/GaInAs (0.75 eV) or GaSb [142, 143]. The difficulties in implementing these stacks are associated with making the upper cell very transparent to the sub-band gap light (use of a transparent GaAs substrate, nonconventional approach for the back contact, and a good AR coating on the back, as well as the front, of the upper cell) and with finding a way to mount both cells with simultaneous heat sinking and electrical isolation, a much greater problem at 500 to 1000X than at 10 to 50X. An advantage of this approach is the decoupling of the photocurrents of the two pieces (assuming that four-terminal measurements are made), allowing for greater flexibility in the choice of materials and higher efficiency when the spectrum is changed [99].

The efficiency of a solar cell depends on the operating conditions, complicating the prediction of outdoor performance of solar cells. This is especially complicated for series-connected, multijunction solar cells under variable spectra. The losses expected for two-terminal operation of three- and four-junction cells, compared with six- or eight-terminal operation of the same cells are significant, but may not be much more than the loss that a silicon cell experiences by operating at elevated temperature [29]. For two-terminal operation, the mechanical stack may most easily be accomplished by bonding the two semiconductor materials directly. Because wafer bonding is now routinely used for integrating many devices, techniques are available, and the wafer bond avoids the need to use a transparent substrate, avoids reflection losses, and removes the difficulty of heat sinking and electrically isolating the stacked cells. If a method for reusing the substrate can be made economical, wafer bonding also has the potential to reduce the substrate cost.

There are many more approaches to making a multijunction cell than can be discussed in this chapter. All approaches are variations on the structures shown in Figure 9.4. Wafer bonding of III-V multijunction cells to silicon would provide a lighter substrate (an advantage for space cells) and could reduce the cost if the original substrate could be reused. A method for making a GaAs-Si bond with ohmic character between a GaAs cell and a silicon wafer has been reported [144]. Wafer bonding has not yet been developed for high-yield manufacturing of solar cells, but large-area wafer bonding is a possibility given that eight-inch wafer-bonded silicon-on-insulator substrates are commercially available. The cost of these wafers is currently high (comparable to the cost of four-inch Ge wafers), but may be reduced in the future.

### 9.8.3 Growth on Other Substrates

A silicon-III-V stack may also be made by growing III-V epitaxial layers directly on silicon. Growth of GaAs on Si has always been problematic because of the large lattice mismatch between the two materials. However, growth of a lattice-matched III-V alloy on silicon might be more similar to the growth of GaAs on Ge. Tu and coworkers have reported the growth of AlGaNP alloys with lattice constants similar to silicon, but having band gaps in the range of 1.4 to 1.95 eV [145]. The use of Si as the 1-eV material in a multijunction higher-efficiency stack is compromised by the poor red *QE* of most Si cells, but the lower cost and weight of the silicon substrate might make it attractive even if higher efficiencies are not achieved.

High efficiencies have been achieved with two-junction (InP/GaInAs) structures on InP [18]. A three- or four-junction structure based on InP could, potentially, achieve

higher efficiencies. This approach is limited by the availability of high band gap materials that are lattice matched to InP and by the weight and current cost of the InP substrates.

### 9.8.4 Spectrum Splitting

Over the years, a number of groups have proposed to separate the light, shining each portion on a solar cell optimized for that wavelength range. If four or five single-junction solar cells are used, the theoretical efficiency is quite high. However, the balance-of-system issues imply that this approach only makes sense for space missions for which high efficiency is essential, and the economics allow for the added cost of multiple substrates without requiring a high concentration ratio.

## 9.9 IMPLEMENTATION INTO TERRESTRIAL SYSTEMS

The implementation of multijunction III-V cells into terrestrial concentrator systems will require appropriate design of the optics, optical coupling between the optics and cells, avoidance of chromatic aberration problems, heat sinking of the cells, electrical connections/isolation, and large-scale production to reduce the cost to an acceptable range.

### 9.9.1 Economic Issues

The current economics imply that the cells should be implemented in a system with a concentration of about 400X or higher. The cell cost is estimated to be in the range of \$3 to 10/cm<sup>2</sup> [146]. Swanson estimates that the cost of electricity from a medium-sized dish-concentrator PV plant in Albuquerque, New Mexico, would be 7 to 15 cents/kWh [13]. He assumed that the cell cost would be \$3 to 10/cm<sup>2</sup>, with an efficiency of 28.5 to 33.25% and a concentration ratio of 1000 [13].

### 9.9.2 Concentrator Systems

Several point-focus designs are available or are being developed. Amonix is installing Si-based concentrators using Fresnel lenses and concentration near 250X [147]. Solar Systems is installing reflective dishes using Si solar cell receivers [148]. Spectrolab and Concentrating Technologies are designing a III-V multijunction solar cell receiver for a dish [149]. With the dishes, a key issue is uniformity of the illumination. The solar cells must be connected in series to boost the voltage, but the current that comes out will be determined by the cell illuminated by the smallest amount of sunlight. SunPower is developing a high-concentration, thin (flat-plate-like) concentrator [150]. ENTECH is redesigning their terrestrial concentrator for use with III-V multijunction cells. The Ioffe and Fraunhofer Institutes have joined to design a 130X glass-Fresnel concentrator using III-V cells [151]. A more complete description of concentrator systems is included in Chapter 11. A number of designs for using multijunction cells under low concentration for space applications are reviewed in Chapter 10.



### 9.9.3 Terrestrial Spectrum

The GaInP/GaAs/Ge cells that are currently produced in high volume for space applications require only minor modifications for terrestrial use. Specifically, under concentrated sunlight, the series resistance must be reduced (as discussed above). And because the direct terrestrial spectrum includes less blue light than the AM0 spectrum, the GaInP cell should be thicker so that it generates a photocurrent that approximately equals that generated by the GaAs junction. There is evidence that the AM1.5 direct reference spectrum is seldom observed in locations that are well suited for concentrators [152]. The AM1.5 global reference spectrum is sometimes observed, but more frequently the spectra lie between these two.

The direct spectrum observed at solar noon is usually richer in short-wavelength light, especially when compared with the AM1.5 direct reference spectrum. Therefore, optimization of the performance at solar noon is slightly different than the optimization for annual electricity production. The Module Energy Rating (MER) Procedure (Chapter 16) addresses this question by defining hourly data for different types of days. The highest performance over a day depends on the location, but may be found when cells are optimized for a spectrum between the AM1.5 global and AM1.5 direct spectra [153]. If the performance early and late in the day is the most important, then thicker top cells are better. However, the increased performance late in the day will reduce the power generated at the times when the most power is available; so this is a trade-off that must be evaluated relative to the application.

The sensitivity of the multijunction structures to variable spectrum has been studied theoretically [21, 29], but not yet experimentally. Modeling of the system performance for concentrators using multijunction cells will be more difficult than modeling Si-based modules because of the spectral sensitivity, but the temperature sensitivity is reduced.

Fundamentally, there should be no difficulty with the lifetime of the cells, but in practice, the need for encapsulation and the complexity of the device structure (tunnel junctions and/or use of Ge substrate, which can cause a higher defect density) could lead to challenges in achieving reliable, manufacturable modules.

## REFERENCES

1. Olson J, Gessert T, Al-Jassim M, *Proc. 18<sup>th</sup> IEEE Photovoltaic Specialists Conference*, 552–555 (1985).
2. Fan J, Tsaur B, Palm B, *Proc. 16<sup>th</sup> IEEE Photovoltaic Specialist Conf.*, 692 (1982).
3. Olson J, Kurtz S, Kibbler A, *Proc. 18<sup>th</sup> IEEE Photovoltaic Specialists Conference*, 777 (1988).
4. Kurtz S, Olson J, Kibbler A, *Sol. Cells* **24**, 307 (1988).
5. Kurtz S, Olson J, Kibbler A, *Appl. Phys. Lett.* **57**, 1922–1924 (1990).
6. Olson J, Kurtz S, Kibbler A, Faine P, *Appl. Phys. Lett.* **56**, 623–625 (1990).
7. Kurtz S, Faine P, Olson J, *J. Appl. Phys.* **68**, 1890 (1990).
8. Bertness K *et al.*, *Appl. Phys. Lett.* **65**, 989–991 (1994).
9. Friedman D *et al.*, *Prog. Photovolt.: Res. Appl.* **3**, 47–50 (1995).
10. Kurtz S *et al.*, *Proc. 1<sup>st</sup> World Conference on PV Energy Conversion*, 2108 (1994).
11. Yamaguchi M, Wakamatsu S, *Proc. 25<sup>th</sup> IEEE Photovoltaic Specialists Conference*, 9–11 (1996).

12. Green M *et al.*, *Prog. PV* **9**, 49–56 (2001).
13. Swanson R, *Prog. Photovolt.: Res. Appl.* **8**, 93–111 (2000).
14. King R *et al.*, *Proc. 29<sup>th</sup> IEEE Photovoltaic Specialists Conference*, 776–779 (2002).
15. O'Neill M *et al.*, *Proc. 28<sup>th</sup> IEEE Photovoltaic Specialists Conference*, 1161 (2000).
16. Henry C, *J. Appl. Phys.* **51**, 4494–4500 (1980).
17. Gee J, *Sol. Cells* **24**, 147–155 (1988).
18. Wanlass M *et al.*, *Proc. 22<sup>nd</sup> IEEE Photovoltaic Specialists Conference*, 38–45 (1991).
19. Hovel H, *Solar Cells*, Vol. 11, Academic Press, New York (1975).
20. Nell M, Barnett A, *IEEE Trans. Electron Devices* **ED-34**, 257–266 (1987).
21. Faine P, Kurtz S, Riordan C, Olson J, *Sol. Cells* **31**, 259 (1991).
22. Kurtz S, O'Neill M, *Proc. 25<sup>th</sup> IEEE Photovoltaic Specialists Conference*, 361–364 (1996).
23. Lockhart L, King P, *J. Opt. Soc. Am.* **37**, 689 (1947).
24. Bader G, Ashrit P, Girouard F, Truong V, *Appl. Opt.* **34**, 1684–1691 (1995).
25. Friedman D *et al.*, *Proc. 12<sup>th</sup> NREL Photovoltaic Program Review*, Vol. AIP 306, 521 (1993).
26. Palik E, Addamiano A, in Palik E, Ed, *Handbook of Optical Constants of Solids*, Vol. I, 597–619, Academic Press, San Diego, CA (1998).
27. Cotter T, Thomas M, Tropsch W, in Palik E, Ed, *Handbook of Optical Constants of Solids*, Vol. II, 899–918, Academic Press, San Diego, CA (1998).
28. Andreev V, Grilikhes V, Rumyantsev V, *Photovoltaic Conversion of Concentrated Sunlight*, John Wiley & Sons, Chichester, Sussex (1997).
29. Kurtz S, Olson J, Faine P, *Sol. Cells* **30**, 501 (1991).
30. Gessert T, Coutts T, *J. Vac. Sci. Technol., A* **10**, 2013–2024 (1992).
31. Friedman D, *Proc. 25<sup>th</sup> IEEE Photovoltaic Specialists Conference*, 89–92 (1996).
32. Zhao J, Wang A, Robinson S, Green M, *Prog. Photovolt.* **2**, 221–225 (1994).
33. Lammasniemi J *et al.*, *Proc. Second World Conference and Exhibition on Photovoltaic Energy Conversion*, 1177 (1998).
34. Bertness K *et al.*, *Proc. 12<sup>th</sup> NREL Photovoltaic Program Review Meeting*, Vol. AIP 306, 100 (1993).
35. Olson J, Kibbler A, Kurtz S, *Proc. 19<sup>th</sup> IEEE Photovoltaic Specialists Conference*, 285 (1987).
36. Matthews J, Blakeslee A, *J. Cryst. Growth* **27**, 118 (1974).
37. Madelung O (Ed), *Semiconductors: Group IV Elements and III-V Compounds*, Springer-Verlag, Berlin, Germany (1991).
38. Kudman I, Paff R, *J. Appl. Phys.* **43**, 3760–3762 (1972).
39. Wie C, *J. Appl. Phys.* **66**, 985 (1989).
40. Tanner B, Miles S, Peterson G, Sacks R, *Mater. Lett.* **7**, 239 (1988).
41. Delong M *et al.*, *Appl. Phys. Lett.* **66**, 3185–3187 (1995).
42. Gomyo A *et al.*, *J. Cryst. Growth* **77**, 367–373 (1986).
43. Gomyo A *et al.*, *Appl. Phys. Lett.* **50**, 673 (1987).
44. Kondow M *et al.*, *J. Cryst. Growth* **93**, 412 (1988).
45. Kurimoto T, Hamada N, *Phys. Rev. B* **40**, 3889 (1989).
46. Capaz R, Koiller B, *Phys. Rev. B* **47**, 4044–4047 (1993).
47. Zhang Y, Mascarenhas A, Wang L, *Phys. Rev. Lett.* **63**, 201312 (2000).
48. Mascarenhas A, Olson J, *Phys. Rev. B* **41**, 9947 (1990).
49. Mascarenhas A, Kurtz S, Kibbler A, Olson J, *Phys. Rev. Lett.* **63**, 2108 (1989).
50. Luo J *et al.*, *J. Vac. Sci. Technol. B* **12**, 2552–2557 (1994).
51. Luo J *et al.*, *Phys. Rev. B* **51**, 7603–7612 (1995).
52. Friedman D *et al.*, *Proc. Material Res. Soc. Symp.*, Vol. 280, 493 (1993).
53. Chernyak L *et al.*, *Appl. Phys. Lett.* **70**, 2425–2427 (1997).
54. Friedman D *et al.*, *Appl. Phys. Lett.* **63**, 1774–1776 (1993).
55. Friedman D *et al.*, *Appl. Phys. Lett.* **65**, 878–880 (1994).
56. Schubert M *et al.*, *J. Appl. Phys.* **77**, 3416–3419 (1995).
57. Kato H, Adachi S, Nakanishi H, Ohtsuka K, *Jpn. J. Appl. Phys.* **33**, 186–192 (1994).

58. Kurtz S, Olson J, *Proc. 19<sup>th</sup> IEEE Photovoltaic Specialists Conference*, 823–826 (1987).
59. Lee H, Klein M, Olson J, Hsieh K, *Phys. Rev. B* **53**, 4015–4022 (1996).
60. Iwamoto T, Mori K, Mizuta M, Kukimoto H, *J. Cryst. Growth* **68**, 27 (1984).
61. Ikeda M, Kaneko K, *J. Appl. Phys.* **66**, 5285 (1989).
62. Gomyo A *et al.*, *Jpn. J. Appl. Phys.* **28**, L1330–L1333 (1989).
63. Kurtz S *et al.*, *J. Electron. Mater.* **19**, 825–828 (1990).
64. Goral J, Kurtz S, Olson J, Kibbler A, *J. Electron. Mater.* **19**, 95 (1990).
65. Kurtz S *et al.*, *J. Electron. Mater.* **23**, 431–435 (1994).
66. Watanabe M, Ohba Y, *J. Appl. Phys.* **60**, 1032 (1986).
67. Hotta H, Hino I, Suzuki T, *J. Cryst. Growth* **93**, 618–623 (1988).
68. Scheffer F *et al.*, *J. Cryst. Growth* **124**, 475–482 (1992).
69. Minagawa S, Ishitani Y, Tanaka T, Kawanaka S, *J. Cryst. Growth* **152**, 251–255 (1995).
70. Wang C *et al.*, *Jpn. J. Appl. Phys.* **34**, L1107–L1109 (1995).
71. Malacky L *et al.*, *Appl. Phys. Lett.* **69**, 1731–1733 (1996).
72. Suzuki M *et al.*, *J. Cryst. Growth* **115**, 498–503 (1991).
73. Kurtz S, Olson J, Kibbler A, Asher S, *Proc. of the InP and Related Materials Conf.* (1992).
74. Suzuki T *et al.*, *Jpn. J. Appl. Phys.* **27**, L1549–L1552 (1988).
75. Nishikawa Y, Ishikawa M, Tsuburai Y, Kokubun Y, *J. Cryst. Growth* **100**, 63–67 (1990).
76. Kurtz S *et al.*, *Proc. 25<sup>th</sup> IEEE Photovoltaic Specialists Conference*, 37–42 (1996).
77. Dabkowski F *et al.*, *Appl. Phys. Lett.* **52**, 2142–2144 (1988).
78. Minagawa S, Kondow M, Yanagisawa H, Tanaka T, *J. Cryst. Growth* **118**, 425–429 (1992).
79. Hino I *et al.*, *Inst. Phys. Conf. Ser. No. 79* **79**, 151–156 (1985).
80. Kondo M, Anayama C, Sekiguchi H, Tanahashi T, *J. Cryst. Growth* **141**, 1–10 (1994).
81. Bauhuis G, Hageman P, Larsen P, *J. Cryst. Growth* **191**, 313–318 (1998).
82. Stockman S *et al.*, *J. Electron. Mater.* **28**, 916–925 (1999).
83. Bertness K, Kurtz S, Asher S, Reedy R, *J. Cryst. Growth* **196**, 13–22 (1999).
84. Kibbler A, Kurtz S, Olson J, *J. Cryst. Growth* **109**, 258 (1991).
85. Friedman D, Kibbler A, Reedy R, *Appl. Phys. Lett.* **71**, 1095–1097 (1997).
86. Ishitani Y *et al.*, *J. Appl. Phys.* **80**, 4592–4598 (1996).
87. Sugira H, Amano C, Yamamoto A, Yamaguchi M, *Jpn. J. Appl. Phys. Pt. 1* **27**, 269 (1988).
88. Friedman D, Kurtz S, Kibbler A, Olson J, *Proc. 22<sup>nd</sup> IEEE Photovoltaic Specialists Conference*, 358–360 (1991).
89. Rafat N *et al.*, *Proc. First World Conference on Photovoltaic Energy Conversion*, 1906–1909 (1994).
90. Karam N *et al.*, *Sol. Energy Mater. Sol. Cells* **66**, 453–466 (2001).
91. Chiang P *et al.*, *Proc. 28<sup>th</sup> IEEE Photovoltaic Specialists Conference*, 1002 (2000).
92. Kadoiwa K *et al.*, *J. Cryst. Growth* **145**, 147–152 (1994).
93. Takamoto T, Agui E, Ikeda E, Kurita H, *Proc. 28<sup>th</sup> IEEE Photovoltaic Specialists Conference*, 976 (2000).
94. Aspnes D, Studna A, *Phys. Rev. B* **27**, 985–1009 (1983).
95. Kim C, Garland J, Raccach P, *Phys. Rev. B* **47**, 1876–1888 (1993).
96. Olson J *et al.*, *Appl. Phys. Lett.* **55**, 1208 (1989).
97. Kurtz S, Olson J, Kibbler A, *Proc. Twenty First IEEE Photovoltaic Specialists Conference*, 138–140 (1990).
98. Oshea J *et al.*, *Appl. Phys. Lett.* **69**, 3022–3024 (1996).
99. Kurtz S, Myers D, Olson J, *Proc. 26<sup>th</sup> IEEE Photovoltaic Specialists Conference*, 875–878 (1997).
100. Friedman D *et al.*, *Proc. 28<sup>th</sup> IEEE Photovoltaic Specialists Conference*, 965 (2000).
101. Lee J, Kim I, Kwon H, Choe B, *Appl. Phys. Lett.* **62**, 1620–1622 (1993).
102. Yoon I, Han S, Park H, Kim T, *J. Phys. Chem. Solids* **62**, 607–611 (2001).
103. Tobin S *et al.*, *Proc. 20<sup>th</sup> IEEE Photovoltaic Specialist Conf.*, 405–410 (1988).
104. Olson J, McMahon W, *Proc. 2<sup>nd</sup> World Conf. on Photovoltaic Energy Conversion* (1998).

105. Pelosi C *et al.*, *J. Electron. Mater.* **24**, 1723–1730 (1995).
106. Li Y *et al.*, *J. Cryst. Growth* **163**, 195–202 (1996).
107. Chen J, Ristow M, Cubbage J, Werthen J, *J. Electron. Mater.* **21**, 347–353 (1992).
108. McMahon W, Olson J, *Phys. Rev. B: Condens. Matter* **60**, 2480–2487 (1999).
109. McMahon W, Olson J, *Phys. Rev. B: Condens. Matter* **60**, 15999–16005 (1999).
110. Sze S, *Physics of Semiconductor Devices*, Wiley, New York, NY (1969).
111. Jung D, Parker C, Ramdani J, Bedair S, *J. Appl. Phys.* **74**, 2090–2093 (1993).
112. Flemish J, Jones K, *J. Electrochem. Soc.* **140**, 844–847 (1993).
113. Lothian J *et al.*, *J. Vac. Sci. Technol. B* **10**, 1061–1065 (1992).
114. Lothian J, Kuo J, Ren F, Pearton S, *J. Electron. Mater.* **21**, 441–445 (1992).
115. Andersson B, *Prog. Photovolt.* **8**, 61–76 (2000).
116. Blood P, *Semicond. Sci. Technol.* **1**, 7–27 (1986).
117. Ahrenkiel R, *Solid State Electron.* **35**, 239–250 (1992).
118. Ahrenkiel R, in Ahrenkiel R, Lundstrom M, Eds, *Minority Carriers in III – V Semiconductors: Physics and Applications*, Vol. 39, 39–150, Academic Press, San Diego, CA (1993).
119. Berger H, *J. Electrochem. Soc.* **119**, 507–514 (1972).
120. Kurtz S, Emery K, Olson J, *Proc. First World Conference on Photovoltaic Energy Conversion*, 1733–1737 (1994).
121. King D, Hansen B, Moore J, Aiken D, *Proc. 21<sup>st</sup> IEEE Photovoltaic Specialists Conference*, 1197 (2000).
122. King R *et al.*, *Proc. 28<sup>th</sup> IEEE Photovoltaic Specialists Conference*, 998 (2000).
123. Cotal H *et al.*, *Proc. 28<sup>th</sup> IEEE Photovoltaic Specialists Conference*, 955 (2000).
124. Takamoto T, Agui T, Ikeda E, Kurita H, *Sol. Energy Mater. Sol. Cells* **66**, 511–516 (2001).
125. King R *et al.*, *Proc. 28<sup>th</sup> IEEE Photovoltaic Specialists Conference*, 982 (2000).
126. Bett A *et al.*, *Proc. 28<sup>th</sup> IEEE Photovoltaic Specialists Conference*, 961 (2000).
127. Dimroth F, Lanyi P, Schubert U, Bett A, *J. Electron. Mater.* **29**, 42–46 (2000).
128. Sinharoy S *et al.*, *Proc. 28<sup>th</sup> IEEE Photovoltaic Specialists Conference*, 1285 (2000).
129. Partain L *et al.*, *21<sup>st</sup> IEEE Photovoltaic Specialists Conference* 184–189 (1990).
130. Schultz J *et al.*, *J. Electron. Mater.* **22**, 755–761 (1993).
131. Timmons M, private communication.
132. Asahi H *et al.*, *J. Cryst. Growth* **175**, 1195–1199 (1997).
133. Friedman D, Kurtz S, Kibbler A, *Proc. NREL/SNL PV Program Review Meeting*, 401–405 (1998).
134. Antonell M *et al.*, *Proc. InP and Related Materials Conf.* 444–447 (1997).
135. Geisz J *et al.*, *Appl. Phys. Lett.* **76**, 1443–1445 (2000).
136. Geisz J, Friedman D, Kurtz S, *Proc. 28<sup>th</sup> IEEE Photovoltaic Specialists Conference*, 990 (2000).
137. Kondow M *et al.*, *Jpn. J. Appl. Phys.* **35**, 1273–1275 (1996).
138. Geisz J *et al.*, *J. Cryst. Growth* **195**, 401–408 (1998).
139. Kurtz S, Allerman A, Jones E, Gee J, Banas J, Hammons B, *Appl. Phys. Lett.* **74**, 729–731 (1999).
140. Friedman D, Geisz J, Kurtz S, Olson J, *J. Cryst. Growth* **195**, 409–415 (1998).
141. Miyamoto T *et al.*, *J. Cryst. Growth* **209**, 339–344 (2000).
142. Moto A, Tanaka S, Tanabe T, Takagishi S, *Sol. Energy Mater. Sol. Cells* **66**, 585–592 (2001).
143. Fraas L *et al.*, *Proc. 28<sup>th</sup> IEEE Photovoltaic Specialists Conference*, 1150 (2000).
144. Arokiaaraj J *et al.*, *Sol. Energy Mater. Sol. Cells* **66**, 607–614 (2001).
145. Hong Y, Tu C, Photovoltaic for the 21<sup>st</sup> Century, *Proc. 199<sup>th</sup> Meeting Electrochemical Soc.* Vol. 2001-10, 415–422 (2001).
146. Kroll W *et al.*, *Proc. 2<sup>nd</sup> World Conference on PV Energy Conversion*, 3753 (1998).
147. Garboushian V, Roubideaux D, Yoon S, Gunn J, *Proc. 25<sup>th</sup> IEEE Photovoltaic Specialists Conference*, 1373–1376 (1996).

148. Lasich J *et al.*, *Proc. First World Conference on Photovoltaic Energy Conversion*, 1938–1941 (1994).
149. Kurtz S, McConnell R, *Compound Semicond.* **7**, 82, 83 (2001).
150. Terao A *et al.*, *Proc. 28<sup>th</sup> IEEE Photovoltaic Specialists Conference*, 1416 (2000).
151. Rumyantsev V *et al.*, *Proc. 28<sup>th</sup> IEEE Photovoltaic Specialists Conference*, 1169 (2000).
152. Myers D *et al.*, *Proc. 28<sup>th</sup> IEEE Photovoltaic Specialists Conference*, 1202 (2000).
153. McMahon W, Kurtz S, Emery K, Young M, *Proc. 29<sup>th</sup> IEEE Photovoltaic Specialists Conference* 931–934 (2002).